CHAPTER
10

Surface-Scattering Models and Land Observations

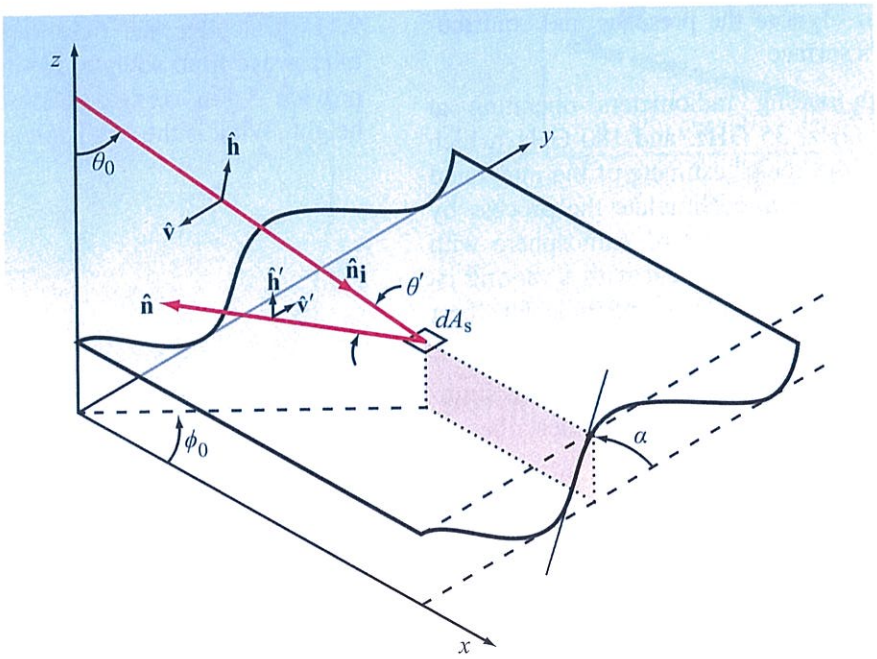

Surface scattering

CONTENTS

Overview

10-1 The role of scattering models

10-2 Surface parameters

10-3 Surface-scattering models

10-4 Scattering by random and periodic surfaces

10-5 PRISM (Polarimetric Radar Inversion for Soil Moisture)

10-6 SMART (Soil Moisture Assessment Radar Technique)

10-7 Model comparisons

10-8 Concluding observations

Overview

The backscattered signal intercepted by a radar observing a ground pixel is a result of either ***surface scattering***, ***volume scattering***, or some combination of both. Scattering by the air-soil interface in Fig. 10-1(a) generates surface scattering, which may be the result of ***single-scattering*** by facets oriented such that their surface normal points towards the radar, ***multiple scattering*** involving reflections by multiple facets, or by resonant effects with particular sinusoidal components of the surface shape. A vegetation canopy [Fig. 10-1(b)] is considered a volume-scattering medium because the layer between the soil surface and the top of the canopy contains many individual scatterers in the form of leaves, needles, and branches. The backscatter from vegetation often includes a component due to scattering by the soil surface as well as multiple scattering involving both the soil surface and the canopy constituents. The third example diagrammed in Fig. 10-1(c) is a snow layer over a soil surface. In this case, the backscatter may include scattering by the upper surface if it is sufficiently rough, volume scattering by the ice crystals within the air background, surface scattering by the lower soil surface, and multiple scattering involving the two interfaces and the snow volume between them.

The focus of this chapter is surface scattering, to be followed with a treatment of volume scattering in Chapter 11. We offer the reader an overview of scattering models for surfaces, supplemented with numerous examples of experimental measurements. The intent is to illustrate the backscatter behavior as a function of the radar wave parameters—namely, the wavelength, incidence angle and receive/transmit polarization configuration—and the surface's geometrical and dielectric properties. We should caution, however, that this is not a chapter about the mathematical techniques used in the development of scattering models. Such an endeavor would consume one or more book volumes all on its own. We refer the reader, instead, to the books by Tsang et al. (1985), Jin (1993), and Fung (1994).

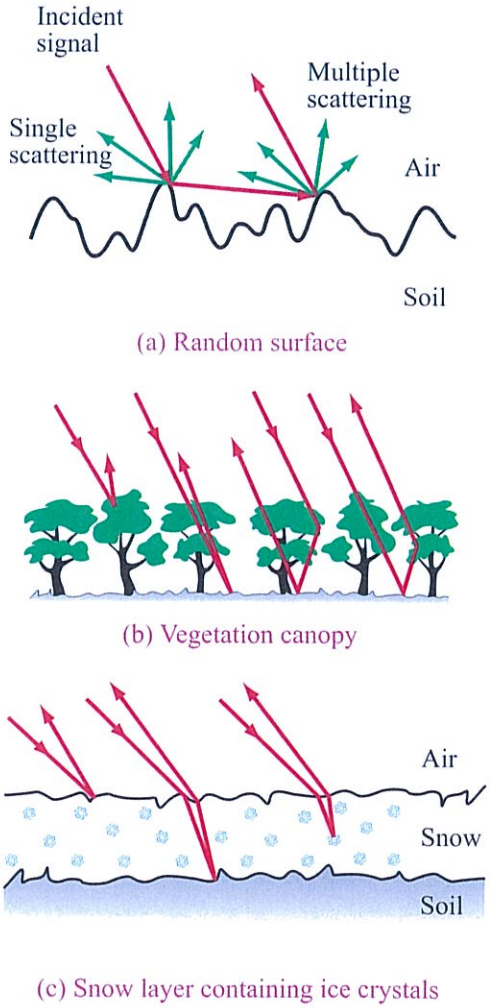

Figure 10-1: Scattering from a random surface, a vegetation canopy, and snow-covered soil.

10-1 The Role of Scattering Models

The geometry of most natural terrain is a superposition of two factors, a quasi-deterministic shape and a random shape variation. The surface of a soil surface has a mean boundary, added to which are random height deviations. A tree canopy contains scatterers with specific shapes, but their sizes and orientations are characterized by probability distributions. Similar statements apply to other types of terrain. The combination of the statistical

nature of terrain targets and the complexity of their shapes makes the task of modeling bistatic scattering from terrain a daunting endeavor. Even a bare soil surface is a challenge to model; capturing the exact profile of the surface geometry is almost impossible, and even if we could do that so as to test the validity of a theoretical model, extending the results to other surfaces (about which we often have little or no information) would be very difficult if not impossible. *So, how do we approach the task of developing scattering models?* The answer is:

(1) We try to describe the terrain in terms of statistical distributions—such as height and slope distributions for a random surface, size and orientation distributions for volume scatterers, etc., and

(2) We perform a mathematical averaging process equivalent to (a) generating a large number of synthesized surfaces and volumes based on the assumed statistics, (b) computing for each synthesized target the scattering cross section for the radar wave parameters of interest, and then (c) performing an ensemble average. Step 2 is equivalent to implementing a Monte-Carlo simulation, but it is carried out mathematically by injecting the assumed statistical distributions into the scattering formulation and then calculating the mean radar cross section.

► Hence, scattering models of terrain are, at best, good approximations of the true scattering process experienced by a real radar observing a real terrain surface or volume. They serve as guides to explain experimental observations and as predictors of how the radar scattering coefficient σ^0 is likely to behave as a function of a particular terrain parameter of interest. ◄

We should note that scattering models are useful not only for radar remote sensing, but also for modeling and understanding the terrain emission observed by a microwave radiometer. As noted in Section 6-7.3, the emissivity of terrain is computed by integrating the bistatic scattering coefficient over all scattering directions [Eq. (6.105)].

10-2 Surface Parameters

As a prelude to the presentations contained in succeeding sections of this chapter, we now introduce (or reintroduce) the principal terminology associated with the physical and statistical properties of natural surfaces.

A given surface that may "appear" very rough to an optical wave may appear very smooth to a microwave. This is because the ***degree of roughness***, or simply the ***roughness***, of a random surface is characterized in terms of statistical parameters, measured in units of wavelength. The two fundamental parameters used to characterize surface roughness are the ***standard deviation of the surface height variation*** (or ***rms height***) s and the surface correlation length l. A third surface parameter that also is important to some surface models is the ***rms slope*** m. In all cases, these statistical parameters are associated with the ***random component*** of surface height, relative to a reference surface. The reference surface may be the unperturbed surface of a deterministic periodic pattern (as in the case of row-tilled soil surfaces or wind-driven ocean waves) as shown in Fig. 10-2(a), or it may be the ***mean surface*** if only random variations exist [Fig. 10-2(b)]. The periodic-surface case is discussed in some detail in Section 10-4.2, so we limit our present discussion to nonperiodic random surfaces.

10-2.1 rms Height

For a random surface whose mean is coincident with the x-y plane, its height $z(x,y)$ above the x-y plane usually is characterized by a Gaussian probability density function $p(z)$ given by

$$p(z) = \frac{1}{\sqrt{2\pi s^2}}\, e^{-z^2/2s^2}, \tag{10.1}$$

where s is the ***rms height***:

$$s = \langle z^2 \rangle^{1/2} = \left[\int_{-\infty}^{\infty} z^2\, p(z)\, dz\right]^{1/2}. \tag{10.2}$$

As noted earlier in Section 5-10.1, the Gaussian assumption is a very good approximation for most natural random surfaces.

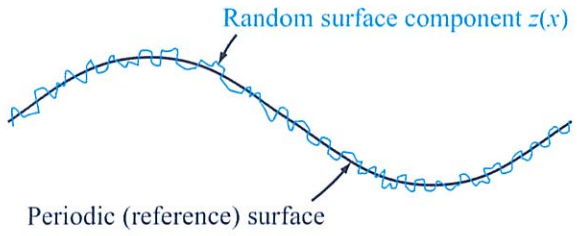

(a) Random height variations superimposed on a periodic surface

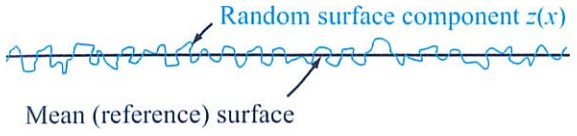

(b) Random height variations superimposed on a flat surface

Figure 10-2: Two configurations of height variations: (a) random height variations superimposed on a periodic surface, and (b) random height variations superimposed on a flat surface.

Alternatively, if $z(x,y)$ of a statistically representative segment of the surface, of dimensions L_x and L_y, centered at the origin, is available, the mean height $\bar{z}$ and second moment $\overline{z^2}$ can be calculated from

$$\bar{z} = \frac{1}{L_x L_y} \int_{-L_x/2}^{L_x/2} \int_{-L_y/2}^{L_y/2} z(x,y)\, dx\, dy, \tag{10.3a}$$

and

$$\overline{z^2} = \frac{1}{L_x L_y} \int_{-L_x/2}^{L_x/2} \int_{-L_y/2}^{L_y/2} z^2(x,y)\, dx\, dy. \tag{10.3b}$$

The rms height is then given by

$$s = (\overline{z^2} - \bar{z}^2)^{1/2}. \tag{10.4}$$

If the surface is azimuthally symmetrical, a one-dimensional height profile $z(x)$ is sufficient, in which case the integration over y is not necessary. In practice, the profile is digitized into discrete values $z_i(x_i)$ at an appropriate spacing Δx. If the height variation Δz corresponding to a horizontal segment Δx is much smaller than the EM wavelength λ, Δz exercises little or no appreciable effect on the reflection by the surface of segment Δx. As a rule of thumb, the spacing Δx should be chosen such that $\Delta x \leq 0.1\lambda$.

The rms height of the discrete one-dimensional case is

$$s = \left[\frac{1}{N-1} \left(\sum_{i=1}^{N} z_i^2 - N\bar{z}^2 \right) \right]^{1/2}, \tag{10.5}$$

where N is the number of samples and

$$\bar{z} = \frac{1}{N} \sum_{i=1}^{N} z_i. \tag{10.6}$$

10-2.2 Surface Correlation Length

The correlation function of the continuous random surface, $\rho(\xi)$, was defined by Eq. (5.105). For the discrete, one-dimensional case,

$$\rho(\xi) = \frac{\sum_{i=1}^{N+1-j} z_i\, z_{j+i-1}}{\sum_{i=1}^{N} z_i^2}, \tag{10.7}$$

where $\xi = (j-1)\,\Delta x$ and j is an integer ≥ 1. The ***correlation length*** l is the value of ξ at which $\rho(\xi) = e^{-1}$. Figure 10-3, which was introduced earlier in Chapter 5, provides a graphical description of $z(x)$, $p(z)$, and $\rho(\xi)$ for a real surface.

For a perfectly smooth surface, $l = \infty$.

10-2.3 rms Slope

The slope of $z(x)$ at location x is given by

$$Z_x(x) = \lim_{\Delta x \to 0} \frac{z(x+\Delta x) - z(x)}{\Delta x}. \tag{10.8a}$$

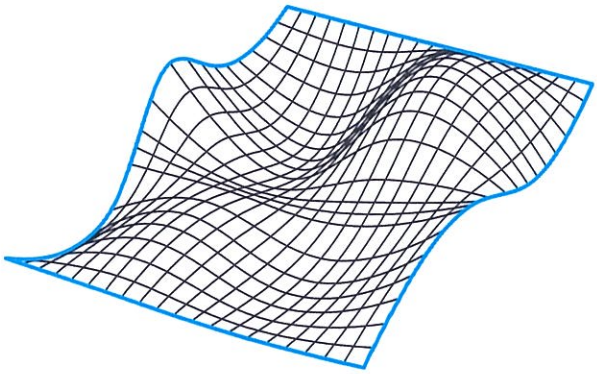

(a) Random surface

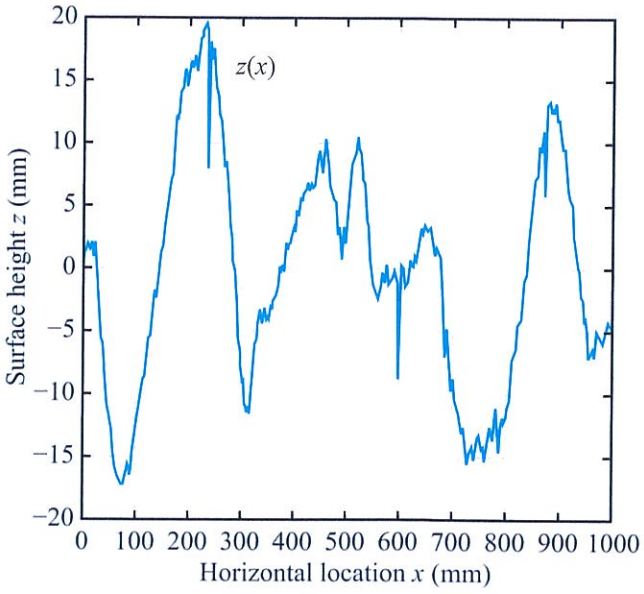

(b) Height profile

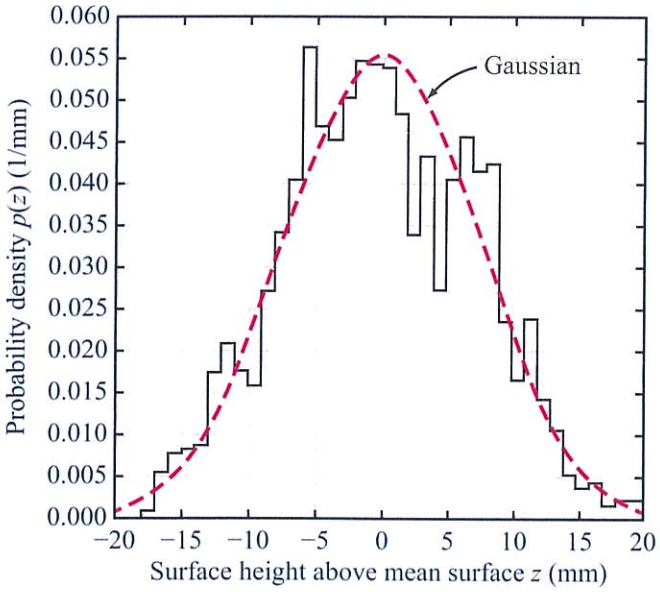

(c) Histogram

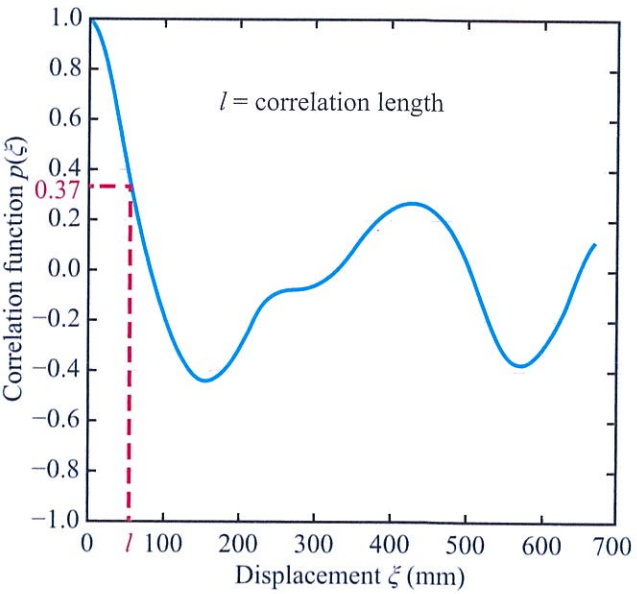

(d) Correlation function

Figure 10-3: Random, isotropic surface $z(x,y)$: (a) pictorial view, (b) measured height profile $z(x)$, (c) pdf of digitized height profile, and (d) autocorrelation function $\rho(\xi)$, where ξ is the displacement between two points on the surface.

The ensemble average of Z_x^2 is

$$\langle Z_x^2 \rangle = \lim_{\Delta x \to 0} \left\langle \frac{z^2(x+\Delta x) - 2z(x)\, z(x+\Delta x) + z^2(x)}{(\Delta x)^2} \right\rangle$$
$$= \lim_{\Delta x \to 0} \left[\frac{s^2 - 2s^2\rho(\Delta x) + s^2}{(\Delta x)^2} \right]$$
$$= 2s^2 \lim_{\Delta x \to 0} \left[\frac{1-\rho(\Delta x)}{(\Delta x)^2} \right], \qquad (10.8b)$$

where s is the rms height and $\rho(\Delta x)$ is the correlation function for separation Δx. To find the limit, we expand $\rho(\Delta x)$ about $\Delta x = 0$ in a Taylor series. Because $\rho(\Delta x)$ is an even function, its first derivative $\rho'(0) = 0$, in which case

$$\langle Z_x^2 \rangle = 2s^2 \lim_{\Delta x \to 0} \left[\frac{1 - [1 + \rho''(0)\,(\Delta x)^2/2 + \cdots]}{(\Delta x)^2} \right]$$
$$\approx -s^2\, \rho''(0), \qquad (10.9)$$

where $\rho''(0)$ is the second derivative of the surface correlation function $\rho(\xi)$ evaluated at $\xi = 0$. The ***rms slope*** is

$$m = \langle Z_x^2 \rangle^{1/2} = [-s^2\, \rho''(0)]^{1/2}. \qquad (10.10)$$

Note that the correlation function is an even function. Hence, $\rho'(0) = 0$ and $\rho''(0)$ is a negative quantity.

10-2.4 Fresnel Reflection Coefficient

The scattering coefficients σ^0_{vv}, σ^0_{hh}, and σ^0_{hv} of a surface are related to the dielectric constant of the surface material, ε, through the Fresnel reflectivities Γ_h, and Γ_v. To first order, σ^0_{vv} is proportional to Γ_v, σ^0_{hh} is proportional to Γ_h, and σ^0_{hv} is related to the product $(\Gamma_v \Gamma_h)^{1/2}$. For soils, ε_{soil} is strongly dependent on the soil's volumetric moisture content m_v. Figure 10-4, extracted from Chapter 4, illustrates the variation of ε_{soil} with m_v at four microwave frequencies. In part (a) of Fig. 10-5, we display the angular variations of $\Gamma_v(\theta)$ and $\Gamma_h(\theta)$ at two moisture contents, and in parts (b) and (c) of the same figure we display the responses of Γ_v and Γ_h, respectively, to m_v at three incidence angles.

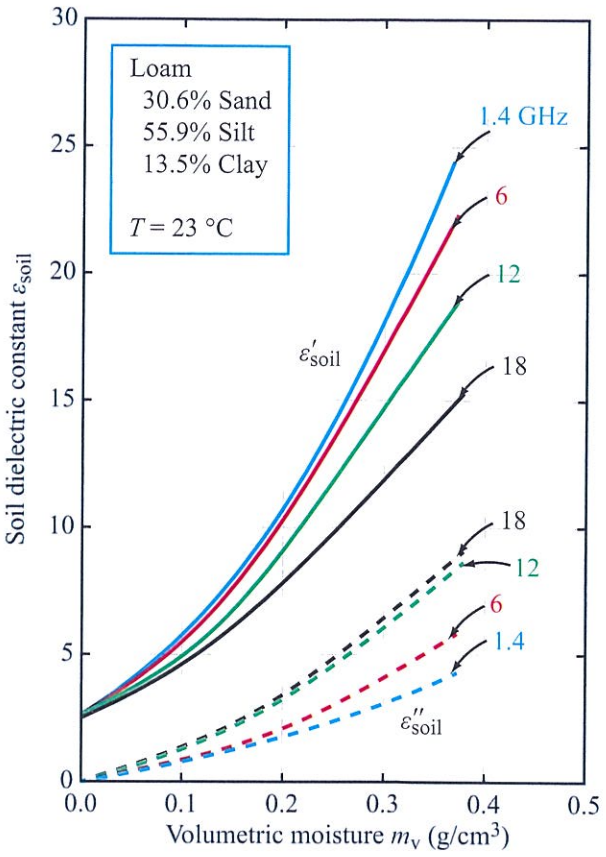

Figure 10-4: Measured dielectric constant as a function of volumetric moisture content for a loamy soil at four microwave frequencies [Hallikainen et al., 1985].

We note that at $\theta = 30°$, for example, Γ_v and Γ_h exhibit a dynamic range of about 4 : 1 (or 6 dB) as m_v is increased from 0.05 g/cm^3 to 0.35 g/cm^3.

10-2.5 Smooth-Surface Criteria

Under what conditions may we consider a surface to be electromagnetically *smooth*?

The geometry shown in Fig. 10-6(a) represents two rays incident normally upon a surface. Had the surface been perfectly flat, the electric fields of the two reflected rays would have been in-phase, but because the rough surface is higher at point B

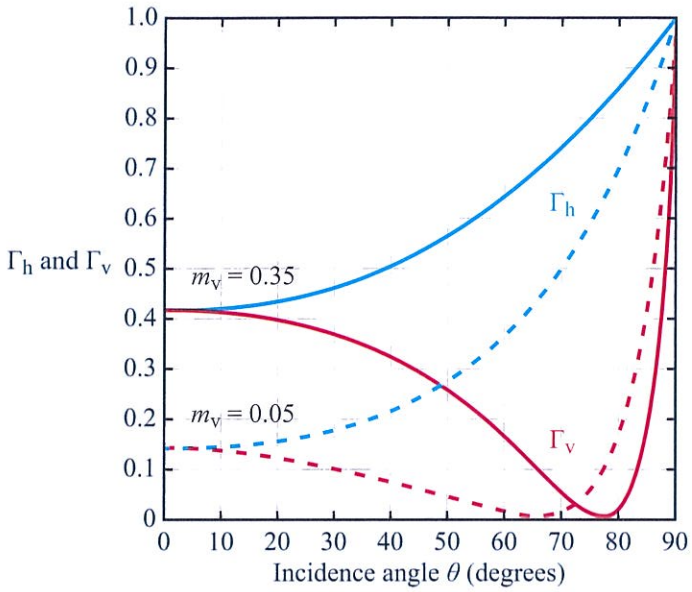

(a) Γ_h and Γ_v versus θ

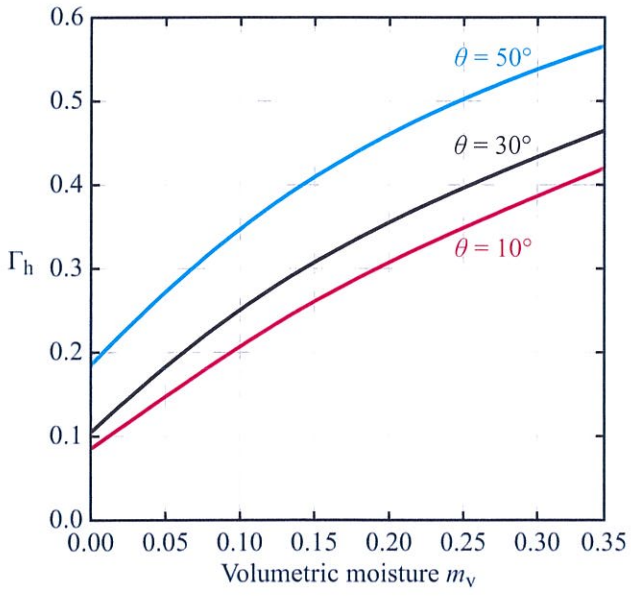

(b) Γ_h versus m_v

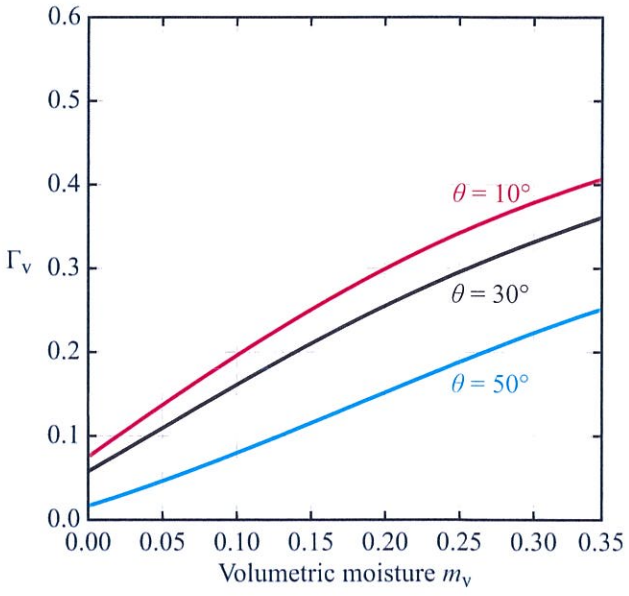

(c) Γ_v versus m_v

Figure 10-5: Variation of reflectivity Γ with θ and m_v for a loamy soil at 1.5 GHz.

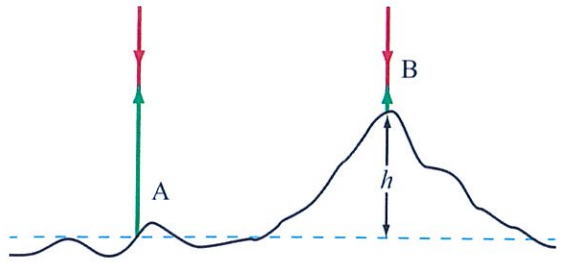

(a) Normal incidence

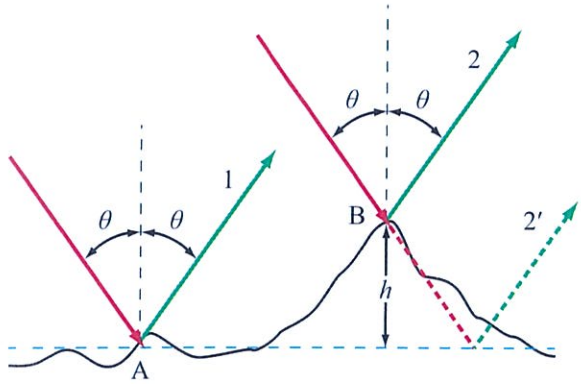

(b) Oblique incidence

Figure 10-6: At (a) normal incidence, the phase difference between the rays reflected from A and B is $\Delta\phi = 2kh$ and at (b) oblique incidence $\Delta\phi = 2kh\cos\theta$.

than at point A by a height h, the field of the ray reflected by point B travels a shorter distance by $2h$. The associated phase difference is $\Delta\phi = 2kh = 4\pi h/\lambda$, where $k = 2\pi/\lambda$ is the wavenumber. For oblique incidence at angle θ [Fig. 10-6(b)],

$$\Delta\phi = 2kh\cos\theta = \frac{4\pi h}{\lambda}\cos\theta. \tag{10.11}$$

The ***Rayleigh roughness criterion*** states that the surface may be considered smooth if $\Delta\phi < \pi/2$, which corresponds to

$$h < \frac{\lambda}{8\cos\theta}.$$

For a random surface with rms surface height s, h may be replaced with s:

$$s < \frac{\lambda}{8\cos\theta} \quad \text{or} \quad ks < 0.8 \quad (\text{at } \theta = 0). \tag{10.12a}$$

(Rayleigh criterion)

The Rayleigh criterion is useful as a first-order classifier of surface roughness or smoothness, but for modeling the scattering and emission behavior of natural surfaces in the microwave region—where the wavelength λ usually is of the order of the rms height s, a more stringent criterion is needed. For this purpose, we adopt the criterion used to define the far-field distance of an antenna, which requires the maximum phase difference between the electric fields of rays coming from the center and the edge of the antenna to be less than $\pi/8$ radians. Such a requirement, which we call the ***Fraunhofer roughness criterion***, leads to the condition

$$s < \frac{\lambda}{32\cos\theta} \quad \text{or} \quad ks < 0.2 \quad (\text{at } \theta_i = 0) \tag{10.12b}$$

(Fraunhofer criterion)

for a surface to be considered smooth. The Fraunhofer criterion is consistent with the results reported earlier in Section 5-10.3 on the coherent reflectivity of a random surface. The dependence of the backscattering coefficient σ^0 on surface roughness is discussed in forthcoming sections of the present chapter, and the dependence of the emissivity on roughness is examined in Chapter 12.

10-3 Surface-Scattering Models

Serious efforts to develop mathematical models for randomly rough surfaces began in the 1950s and culminated in two approximate models. The first one, developed by Rice (1951) for slightly rough surfaces whose rms heights and correlation lengths are both smaller than the incident wavelength, became known as

the ***small perturbation model***. Its validity conditions are:

$$\left.\begin{array}{l} ks < 0.3 \\ kl < 3 \\ \dfrac{s}{l} < 0.3 \end{array}\right\} \quad \textbf{(small perturbation model)},$$

where s is the rms height, l is the correlation length and $k = 2\pi/\lambda$.

The second approximate model, known as the ***Kirchhoff scattering model***, was developed by Beckman and Spizzichino (1963) to describe EM scattering by surfaces with gentle undulations whose average horizontal dimensions are large compared with λ. To evaluate the integral representing the total field scattered by the surface, two types of approximations have been used, one for $ks = (2\pi s/\lambda) \geq 3$, which is then known as the ***geometric optics model***, and another for $ks < 3$, which is known as the ***physical optics model***. The validity conditions include additional constraints related to the average radius of curvature and rms slope of the undulating surface. When $ks \geq 3$ and the radius of curvature of the roughness scale is much larger than a wavelength, the scattering process is dominated by reflection. The correlation function (introduced shortly in Section 10-3.1) can be approximated by the first two terms of its Taylor expansion in the scattered field integral, and this leads to the ***geometric optics model***. When $ks < 3$ and the radius of curvature of the roughness is still larger than a wavelength, then locally both reflection and diffraction are important. In this case, the correlation function cannot be approximated and the resulting model is known as the ***physical optics model***.

► The Kirchhoff model deals with roughness scales that are larger than a wavelength in horizontal extent, while the perturbation model deals with roughness scales that are small relative to the radar wavelength. Clearly, a better surface-scattering model is needed, one that has no restriction on the size of the surface roughness scales. ◄

Across the microwave band, which extends over the wavelength range from 1 mm ($f = 300$ GHz) to 30 cm ($f = 1$ GHz), natural surfaces encompass a wide range of roughness scales. Consequently, the aforementioned 1960s scattering models are applicable over limited segments of the roughness scale of interest. Over the next three decades, many attempts were made to improve the models and extend their regions of validity, culminating in the development of an ***integral equation model*** (IEM) (Fung et al., 1992) capable of bridging the gaps between its various predecessors. The applicability of the model, however, is limited to the backscatter direction. Over the next decade, Fung and his colleagues extended the range of applicability of the IEM to bistatic scattering (Fung et al., 2002). The new model is referred to in this book as the ***improved IEM scattering model***, or I^{2}EM for short.

As mentioned earlier, the emissivity of a rough surface is computed by integrating the total bistatic scattering over the upper hemisphere. The availability of the I^{2}EM makes such a computation viable, as discussed in more detail in Chapter 12.

10-3.1 I^{2}EM Parameters

The I^{2}EM model is a mathematically sophisticated computational algorithm with which one can compute the backscattering or bistatic scattering coefficient of a random surface with any specified degree of roughness for any combination of receive and transmit wave polarizations. The computation includes multiple scattering contributions and accounts for shadowing effects. Generally, multiple scattering from a surface is small (in comparison with single scattering) except for surfaces with large rms slopes, which is uncommon for natural surfaces. When multiple scattering contributions, which require a two-dimensional integration, are excluded, the model reduces to a relatively simple algebraic form. Figure 10-7 provides in block-diagram format the list of surface and radar wave parameters required to specify the model to compute σ^0. Theoretically, correlation functions used in the model should be differentiable at the origin. Hence, the commonly used exponential correlation function is not acceptable. However, for low to medium frequency calculations this property of the correlation function can be relaxed, because the computed result does not depend on this property until

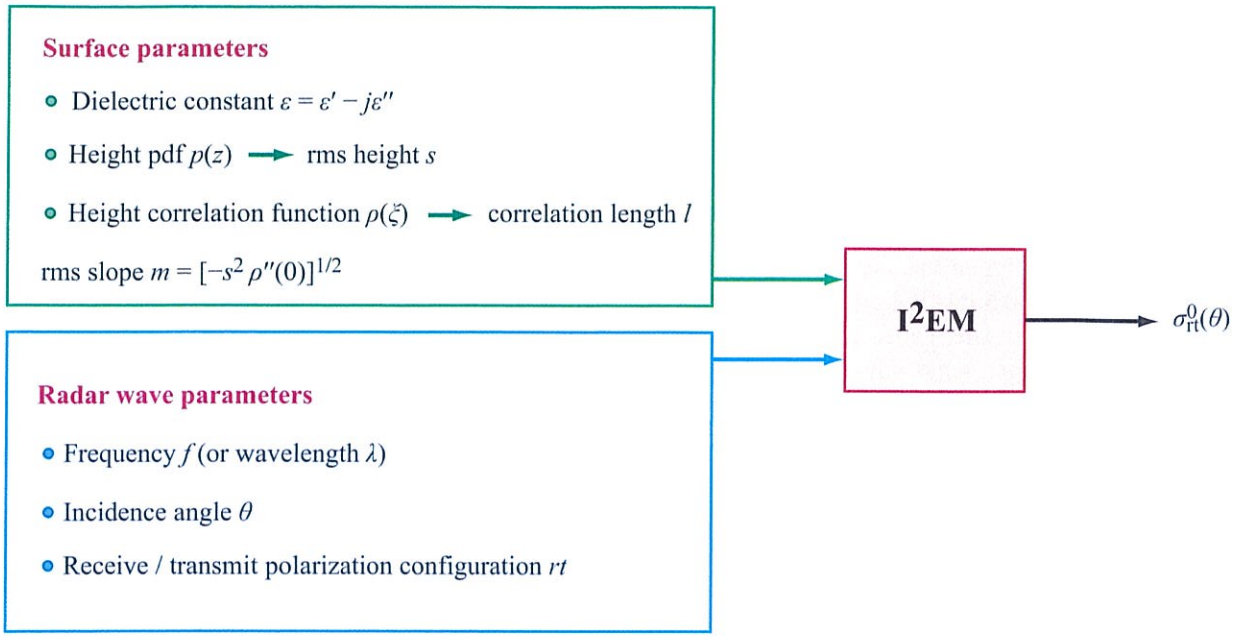

Figure 10-7: Block-diagram representation of the surface and radar input parameters for the I²EM model in the backscatter mode. For bistatic scattering, θ becomes θ_i and the scattered direction is specified by θ_s and ϕ, where ϕ is the azimuth angle between the incident and scattered directions.

we get close to the geometric-optics condition, where all roughness scales are large compared with the incident wavelength. In practice, we rarely reach this high-frequency condition, because natural surfaces normally have many roughness scales. As we shorten the incident wavelength, the wave simply responds to smaller scales. Some of the ***correlation functions*** reported in the literature include:†

$$\textbf{Exponential:} \quad \rho(\xi) = e^{-|\xi|/l} \tag{10.13a}$$

$$\textbf{Gaussian:} \quad \rho(\xi) = e^{-\xi^2/l^2} \tag{10.13b}$$

$$\textbf{x-exponential:} \quad \rho(\xi) = e^{-(|\xi|/l)^x}. \tag{10.13c}$$

$$\textbf{x-power:} \quad \rho(\xi) = \frac{1}{[1 + (\xi^2/l^2)]^x} \tag{10.13d}$$

The four correlation functions represent different approaches on how to characterize the statistical correlation between the height $z(x)$ at location x with the height $z(x + \xi)$ at a location separated from the first location by a distance ξ. Measuring the height profile $z(x)$ of a random surface with a high degree of vertical accuracy across a long horizontal segment and along many different horizontal directions is a difficult and laborious process. Based on the relatively few such measurements reported in the literature for natural surfaces, the exponential correlation function appears to provide the best fit, with the Gaussian a close second. For both the exponential and Gaussian correlation functions, l represents the correlation distance of the random surface, defined as the separation ξ at which $\rho(\xi) = 1/e$ (Section 5-10.1). The x-exponential correlation function is a two-parameter function (x and l) that reduces to the exponential function for $x = 1$ and to the Gaussian for $x = 2$ [Fig. 10-8(a)]. Having two fitting parameters, the x-exponential function provides greater flexibility in matching the model to correlation functions based on measured surface height profiles. Moreover, the value of l in the x-exponential correlation function

† Computer Code 10.1.

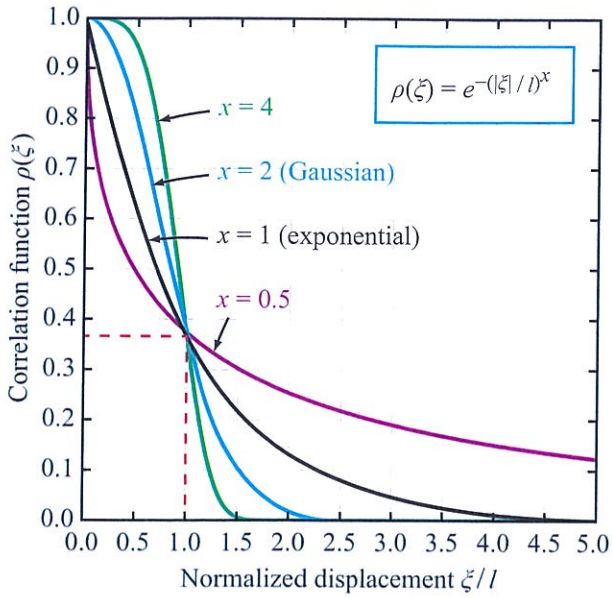

(a) The x-exponential correlation function

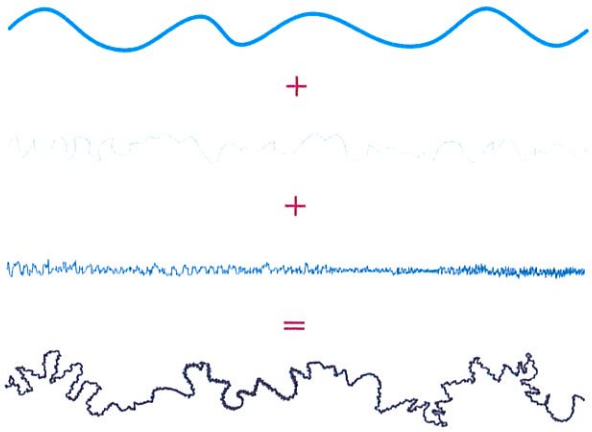

(b) Multiscale roughness

Figure 10-8: (a) x-exponential correlation function and (b) three-scale random surface.

continues to represent the usual definition associated with correlation distance. The last correlation function listed in Eq. (10.13) is the x-power function, which also has two fitting parameters, but in this case l no longer represents the usual definition of the correlation length.

For the x-power and Gaussian correlation functions, the rms slope defined by Eq. (10.10) is given by

$$m = \sqrt{3}\,\frac{s}{l} \quad (x\text{-power with } x = 1.5), \tag{10.14a}$$

$$m = \sqrt{2}\,\frac{s}{l} \quad \text{(Gaussian)}. \tag{10.14b}$$

10-3.2 Multiscale Surfaces

A real random surface consists of multiple, or continuous, scales of roughness, with the smaller scales "riding" on top of the larger scales. Figure 10-8(b) depicts a ***three-scale surface*** consisting of a large-scale undulation with correlation length l_1 and associated rms height s_1, a medium-scale perturbation with l_2 and s_2, and a small-scale high-spatial frequency variation with l_3 and s_3. If we were to measure the height profile $z(x)$ of the composite surface with a sensor (such as a laser beam) capable of measuring $z(x)$ with a precision superior to the smallest scale (i.e., with a vertical resolution $\Delta z \ll s_3$ and a horizontal resolution $\Delta x \ll l_3$), and if the surface correlation is Gaussian, the correlation function derived from the measured record would have the functional form[†]

$$\rho(\xi) = \frac{1}{s^2}[s_1^2 e^{-\xi^2/l_1^2} + s_2^2 e^{-\xi^2/l_2^2} + s_3^2 e^{-\xi^2/l_3^2}], \tag{10.15a}$$

where s, the equivalent rms height of the composite surface, is related to the individual rms heights by

$$s^2 = s_1^2 + s_2^2 + s_3^2. \tag{10.15b}$$

The surface scattering process is subject to a ***wavelength filtering*** effect that, in effect, determines which scales of roughness are important and which are not. Let us examine, qualitatively, what happens as λ is varied from $\lambda \gg l_1$ to $\lambda \ll s_3$. When λ is much longer than s_1 and l_1 of the largest scale, the surface "appears" to the incident wave as if it were perfectly flat, in which case the wave reflects coherently along the specular direction relative to the mean surface, and no incoherent

[†] **Computer Code 10.2.**

scattering occurs along any direction. As the wavelength is made shorter so that it approaches the dimensions of s_1 and l_1 of the largest scale, incoherent scattering does occur, but the shorter scales do not play a significant role. This is what is meant by wavelength filtering. As the dimension of λ approaches the dimensions of s_2 and l_2 of the medium-scale roughness, the scattering process becomes responsive primarily to the medium-scale statistics. Further reduction of λ toward the small scale leads to diminution of the role of the medium- and large-scale roughnesses (except for defining the mean slope upon which the small-scale roughness resides) and to an increased role for the small-scale roughness. An illustration of the scattering behavior just described is shown in Fig. 10-9, where we show backscattering computations at 2, 4, and 9 GHz for a surface with three roughness scales. It is clear from the figure that as either the incident angle or frequency increases, the smaller roughness scales become increasingly important.

At microwave frequencies, λ is on the order of centimeters to a few tens of centimeters. Hence, the centimeter scale is the scale of roughness of primary importance from the standpoint of surface scattering. At $f > 10$ GHz, the millimeter scale starts becoming important, but unfortunately it is very difficult to measure millimeter-scale roughness of natural surfaces.

► Hence, in practice we tend to characterize surfaces by only their centimeter-scale roughness statistics, which occasionally leads to inconsistencies between model-calculated values and experimentally observed values of the backscattering coefficient. The scattering by the real surface involves scattering at multiple scales, whereas the model-calculated scattering is based on single-scale statistics. This is not because the model cannot compute multiscale statistics, but rather because the vertical precision and horizontal spacing of the measured roughness profile are inadequate for recording the millimeter-scale roughness component of the real profile. ◄

The mathematical details of I^{2}EM are outside the scope of this book, but its utility as a guide and predictor of scattering behavior is very much of interest. Hence, in the next few subsections, we use it to examine the roles of surface roughness and dielectric constant and to compare model predictions with experimental measurements.

10-3.3 Role of Correlation Function

In Fig. 10-10 we display angular plots for σ^0_{vv}, σ^0_{hh}, and σ^0_{hv} computed using I^{2}EM for two surfaces with identical parameters, except for their correlation functions. The two surfaces have the same correlation length of 10 cm, but one is characterized by an exponential correlation function, as defined by Eq. (10.13a), and the other is characterized by the Gaussian correlation function of Eq. (10.13b). We observe that for each of the three polarization combinations, σ^0 of the Gaussian surface exhibits a much steeper angular response than does that of the exponential surface. At $\theta = 70°$, σ^0_{hh} (Gaussian) is about 38 dB lower in magnitude than σ^0_{hh} (exponential), and for hv polarization the difference is about 50 dB. These are very large differences; 50 dB corresponds to five orders of magnitude!

► Experimental measurements of σ^0 for soil surfaces with comparable surface conditions (rms height s, correlation length l, and dielectric constant ε) are much closer in level to the predictions of the I^{2}EM for a surface with an exponential correlation function than for a Gaussian. ◄

10-3.4 Role of rms Height s

To illustrate the effect that the rms height s has on the level of σ^0, we used I^{2}EM to generate angular plots of σ^0_{hh}, σ^0_{vv}, and σ^0_{hv} at 3 GHz for two surfaces (Fig. 10-11, one with $s = 0.5$ cm (with a corresponding $ks \approx 0.3$) and a second one with $s = 1.5$ cm (with a corresponding $ks \approx 0.9$). At angles greater than 20°, the co-polarized backscattering coefficients are on the order of 8–15 dB higher for the rougher surface than for the smoother surface, and the difference in level is closer to 17 dB for σ^0_{hv}. In general, at angles greater than 20°, all three

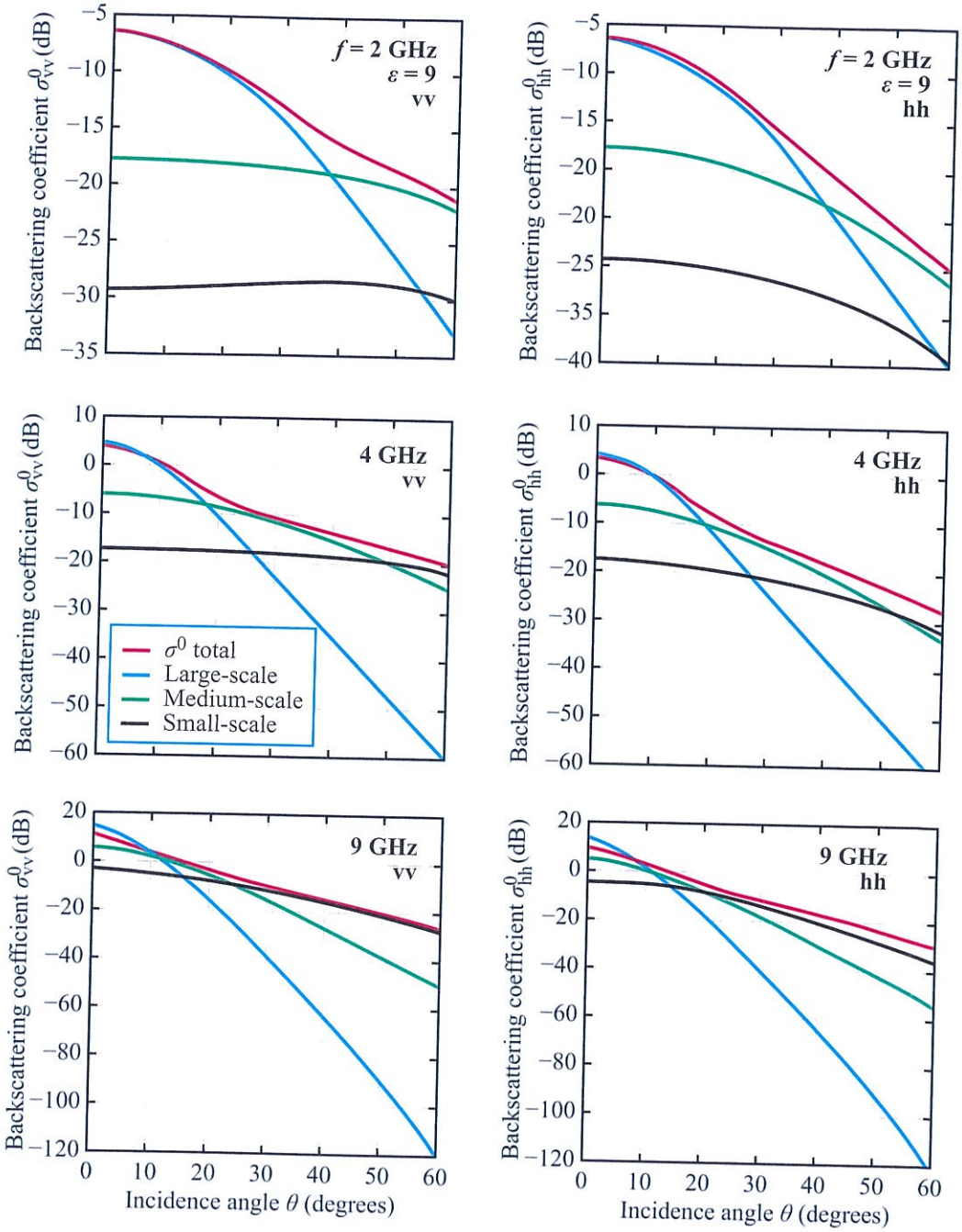

Figure 10-9: In backscattering, the effective wavelength is $\lambda_e = \lambda/(2\sin\theta)$. As λ_e is shortened due to an increase in either frequency or angle, the smaller roughness scales become more effective in scattering. The surface has three roughness scales: large-scale with $(s_1, l_1) = (0.4\text{ cm},\ 7\text{ cm})$, medium-scale with $(s_2, l_2) = (0.25\text{ cm},\ 3\text{ cm})$, and small-scale with $(s_3, l_3) = (0.13\text{ cm},\ 1.5\text{ cm})$. The plots show the individual contributions of the three roughness scales, as well as the total.

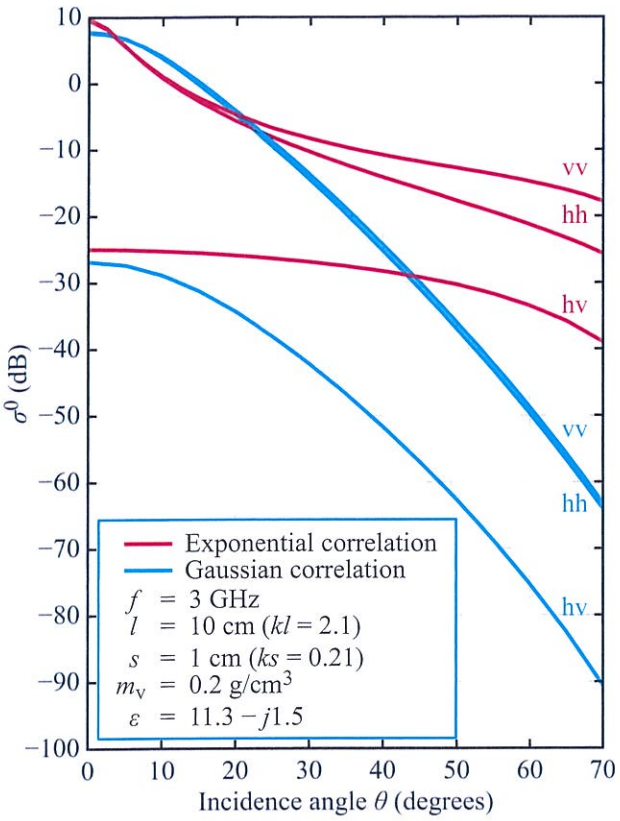

Figure 10-10: I^{2}EM comparison of the backscattering coefficients for two surfaces with identical surface parameters, but different correlation functions.

backscattering coefficients increase with increasing ks (but at different rates) up to about $ks \approx 2$, beyond which their responses approach constant levels (as discussed later in Section 10-3.6).

10-3.5 Role of Correlation Length l

The correlation length l exercises a weaker influence on σ^0 compared with the rms height s; increasing l from 2 cm to 16 cm in Fig. 10-12 causes σ^0 to drop in level by about 5–6 dB for vv and hv polarizations, and by about the same amount for hh polarization (not included in Fig. 10-12 to avoid unnecessary crowding of curves).

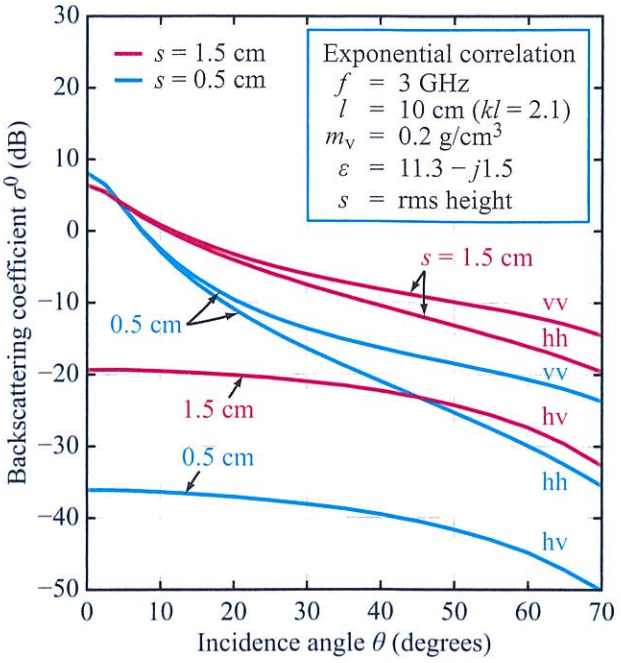

Figure 10-11: I^{2}EM backscatter response to two surfaces with different rms heights.

10-3.6 Role of Dielectric Constant

At 3 GHz, the real part of the dielectric constant of loamy soil increases with volumetric moisture content from about 3 at $m_v \approx 0$ to 20.6 at $m_v = 0.35$ g/cm^3. Figure 10-13(a) displays multipolarization angular plots of σ^0 and Fig. 10-13(b) displays plots of σ^0 as a function of m_v at $\theta = 30°$. Over the full range of m_v, σ^0_{vv} increases by 8 dB, σ^0_{hh} increases 6 dB, and σ^0_{hv} increases 13 dB. Comparable rates are observed at other angles of incidence.

10-3.7 Role of Polarization Ratios

The ***co-polarized*** and ***cross-polarized*** ratios are defined as

$$p = \frac{\sigma^0_{hh}}{\sigma^0_{vv}}, \quad \text{or } p(\text{dB}) = \sigma^0_{hh}(\text{dB}) - \sigma^0_{vv}(\text{dB}), \tag{10.16a}$$

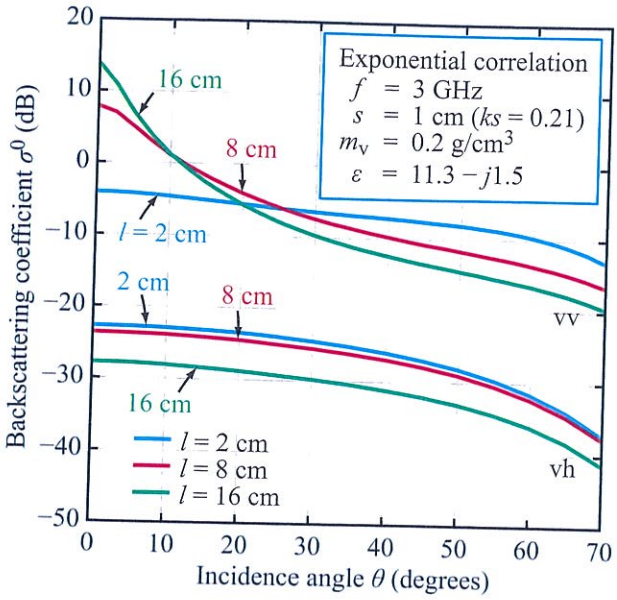

Figure 10-12: The role of the correlation length l is demonstrated by three surfaces with $l = 2$ cm, 8 cm, and 16 cm, all computed using I^{2}EM.

and

$$q = \frac{\sigma^0_{hv}}{\sigma^0_{vv}}, \quad \text{or} \quad q(\text{dB}) = \sigma^0_{hv}(\text{dB}) - \sigma^0_{vv}(\text{dB}). \tag{10.16b}$$

The plots shown in Fig. 10-14 were computed using I^{2}EM at $\theta = 30°$ for a surface with an rms height $s = 1$ cm and correlation length $l = 10$ cm. The backscattering coefficients were calculated as a function of the electromagnetic roughness ks by incrementally increasing the frequency from 1 GHz to 15 GHz. We note the following general trends:

(a) The co-pol ratio p(dB) increases by about 3 dB as ks is increased from 0.25 to 2. As ks is increased beyond 2, p(dB) approaches 0 dB, or $\sigma^0_{hh} = \sigma^0_{vv}$.

(b) The co-pol ratio has a higher level for the lower moisture content of 0.05 g/cm^3 than for the higher moisture content of 0.35 g/cm^3.

(c) The cross-pol ratio q(dB) increases by about 18 dB as ks is increased from 0.25 to 3.

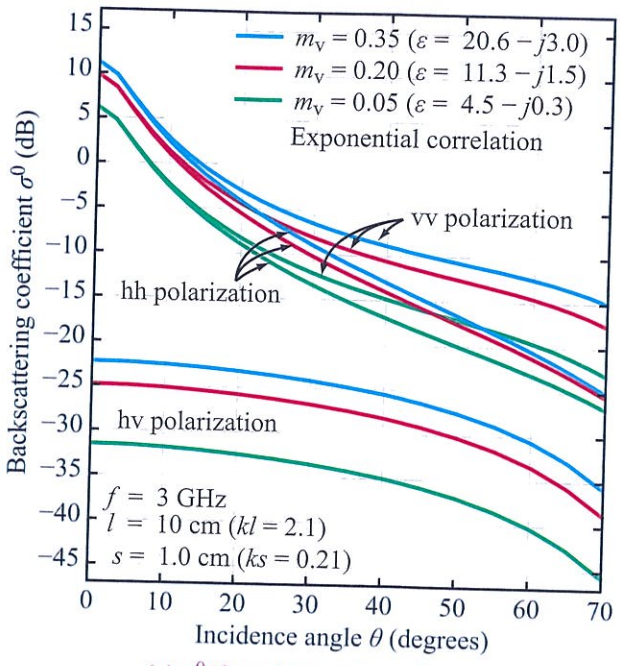

(a) $\sigma^0(\theta)$ at three values of m_v

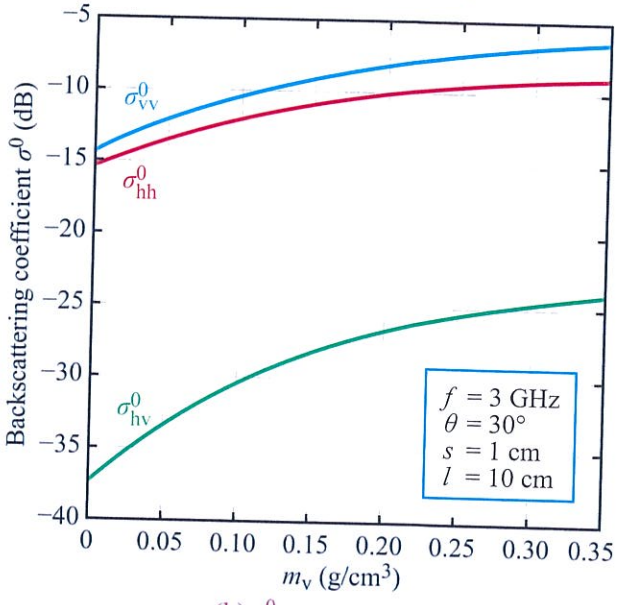

(b) σ^0 versus m_v

Figure 10-13: The role of soil moisture: (a) angular response of σ^0 for three surfaces with different soil moisture content, (b) σ^0 versus m_v at 30°.

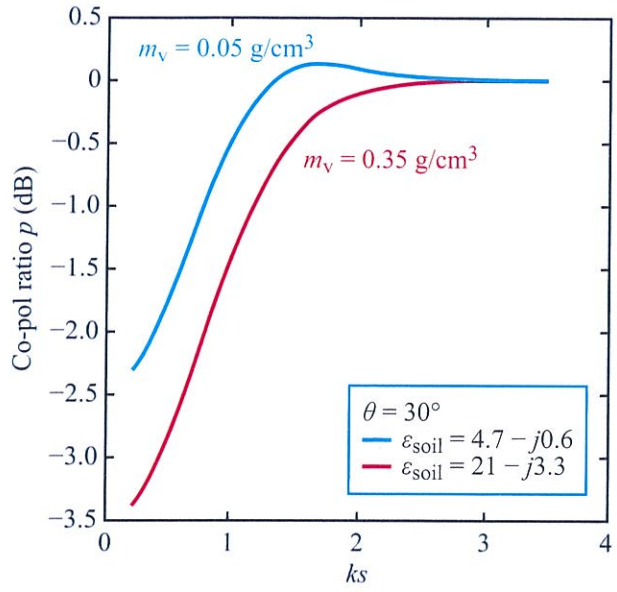

(a) p(dB) versus ks

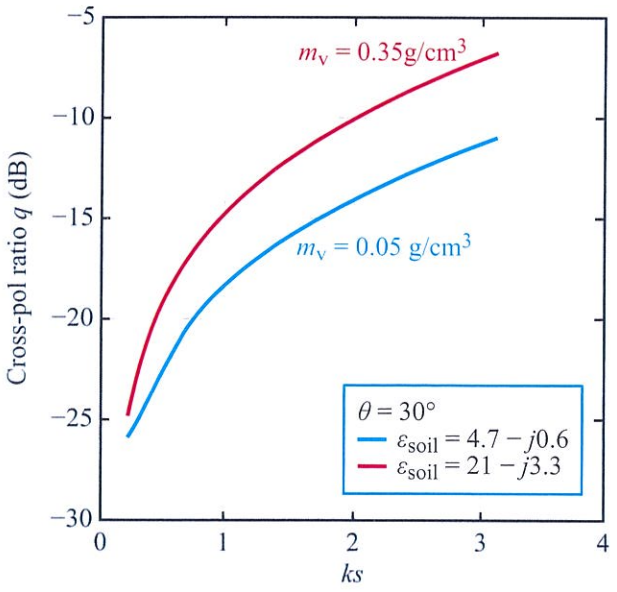

(b) q(dB) versus ks

Figure 10-14: I^{2}EM-computed plots of (a) the co-pol ratio p(dB) and (b) the cross-pol ratio q(dB) as a function of ks.

(d) For q, the role of soil moisture is opposite that for p; q increases with increasing soil moisture, whereas p decreases.

The foregoing general trends of I^{2}EM are all confirmed by the experimental observations presented in Section 10-5.

10-3.8 Comparison with Experimental Backscattering Measurements

By way of illustration, we show in Fig. 10-15 angular plots for σ^0_{vv} and σ^0_{hh} calculated using I^{2}EM, together with experimental measurements reported by Oh et al. (1992) for a relatively smooth random surface with an rms height $s = 0.4$ cm. Good overall agreement is observed between the model-calculated curves and the experimental measurements, at both 1.5 GHz and 4.75 GHz.

A similar set of data is shown in Fig. 10-16 for a rougher surface with $s = 1.12$ cm. Again, the model and the experimental data are in close agreement.

10-3.9 Comparison with Experimental Bistatic Measurements

So far in this section, we examined the behavior of I^{2}EM for the backscattering case only. The model, however, is equally applicable to bistatic scattering, which is critical for computing the emissivity of random surfaces. Recall from Section 6-7.3 that the emissivity of a surface given by Eq. (6.105) is proportional to an integration of the bistatic scattering coefficient over the upper hemisphere. For an isotropic random surface, bistatic scattering involves three angles, the incidence angle θ_i, the scattering angle θ_s, and the azimuth angle $\phi = \phi_s - \phi_i$.

In Fig. 10-17 we display plots of σ^0_{vv} and σ^0_{hh} as a function of θ_i in the ***incidence plane***, defined as $\theta_s = \theta_i$ and $\phi = 0$. The plots correspond to three surfaces with different roughnesses, all measured at 10 GHz by De Roo and Ulaby (1994). Not only does I^{2}EM[†] provide computed values that are in close agreement with the experimental measurements, but it

[†] **Computer Code 10.3.**

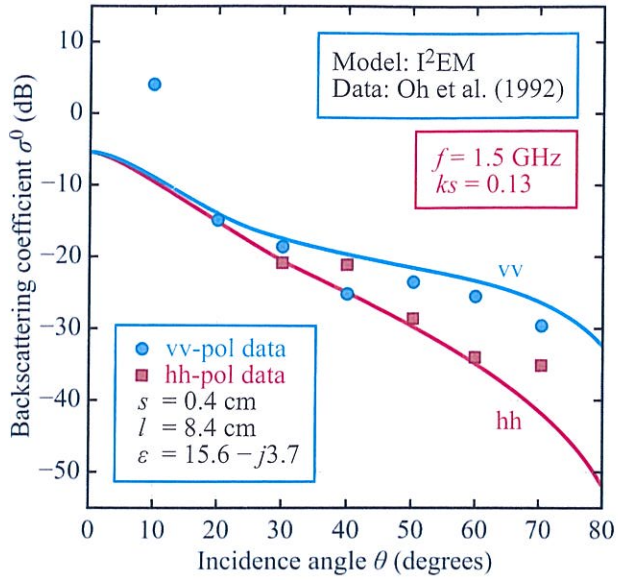

(a) Smooth surface at 1.5 GHz

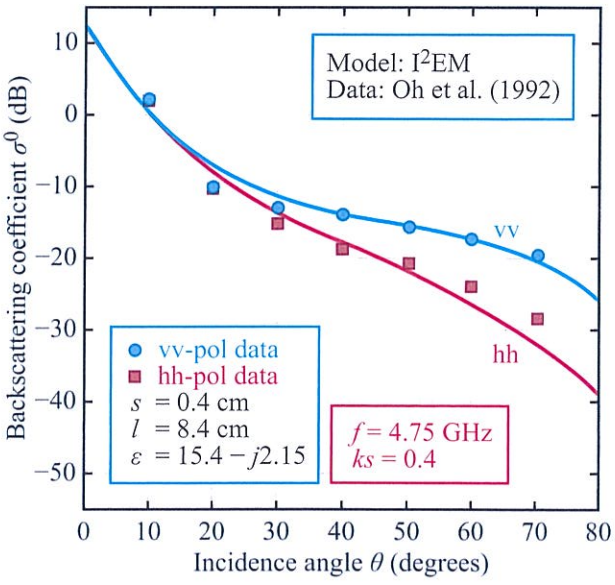

(b) Smooth surface at 4.75 Ghz

Figure 10-15: Comparison of I²EM-calculated values of σ^0 with experimental data measured for a smooth surface with $s = 0.4$ cm.

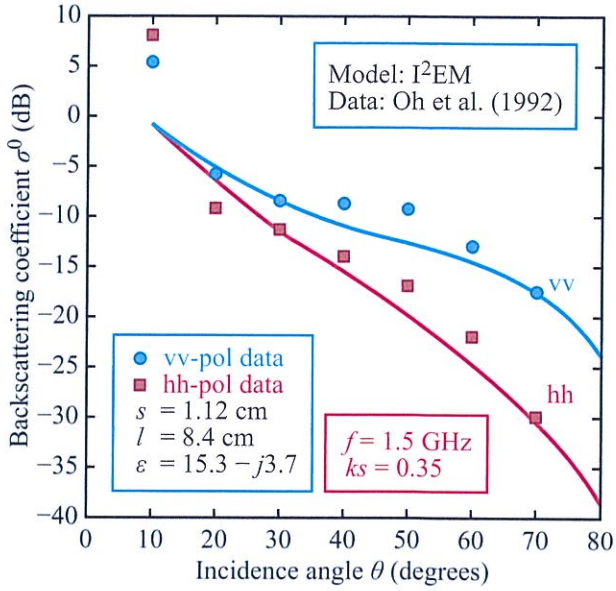

(a) Rough surface at 1.5 Ghz

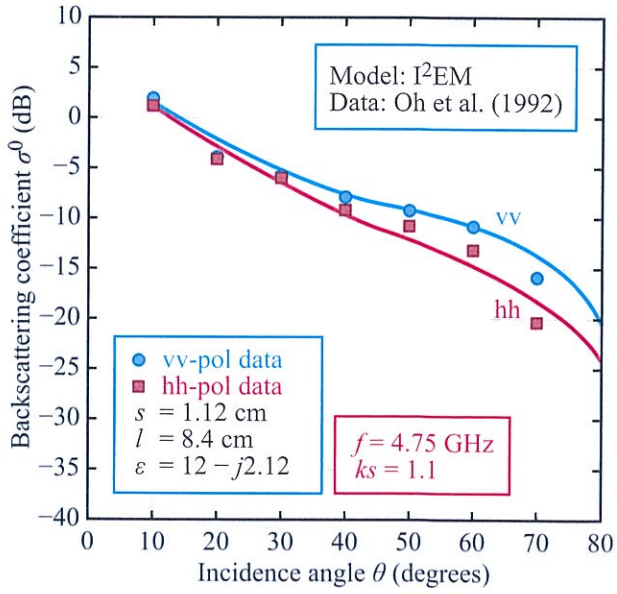

(b) Rough surface at 4.75 GHz

Figure 10-16: Comparison of I²EM-calculated values of σ^0 with experimental data measured for a rough surface with $s = 1.12$ cm.

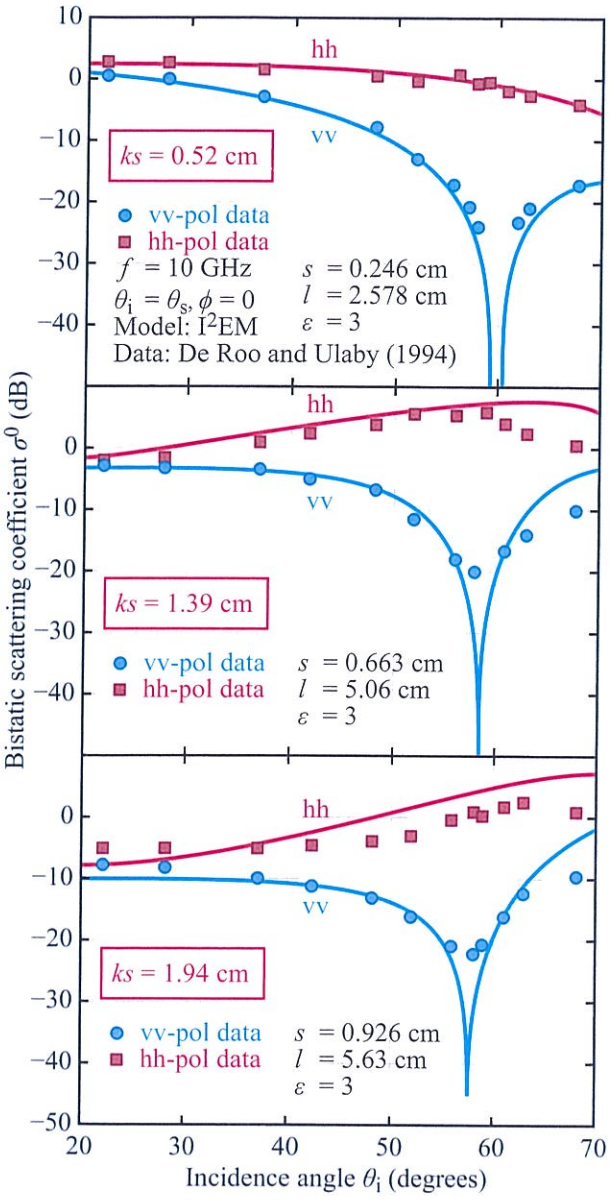

Figure 10-17: Comparison of I²EM-computed bistatic scattering coefficient with measurements made in the incidence plane ($\theta_i = \theta_s$ and $\phi = 0$) for three surfaces with different roughnesses.

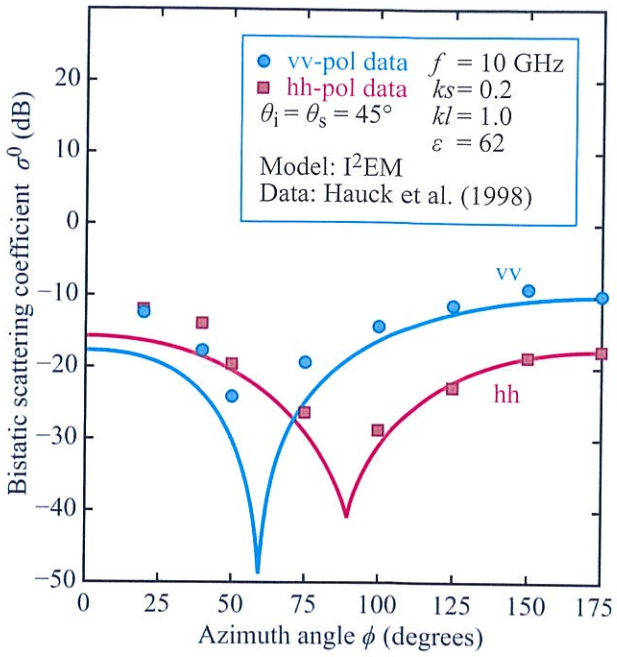

Figure 10-18: Comparison of I²EM-computed bistatic scattering coefficient with measurements made as a function of the azimuth angle ϕ for $\theta_i = \theta_s = 45°$.

also correctly predicts the shift in the location of the Brewster angle from about 60° for the smoothest surface with $s = 0.246$ cm (or $ks = 0.515$) to about 57° for the roughest surface with $s = 0.926$ cm (or $ks = 1.94$).

The variations of σ^0_{hh} and σ^0_{vv} with the azimuth angle ϕ are illustrated in Fig. 10-18 for a relatively smooth random surface with $s = 0.2$ cm observed at 4.775 GHz (Hauck et al., 1998). The incidence and scattering angles are held constant at $\theta_i = \theta_s = 45°$. I²EM correctly predicts the levels of σ^0_{vv} and σ^0_{hh} and their variations with ϕ.

Our last example, presented in Fig. 10-19, pertains to the variations of σ^0_{hh} and σ^0_{vv} as a function of the scattering angle θ_s, while holding the other two angles constant at $\theta_i = 20°$ and $\phi = 0$. The measured data, which were reported by the European Microwave Signature Laboratory of the Joint Research Center in Italy on its website (wmw-emsl.jrc.it), were made for an artificially generated random surface with a Gaussian

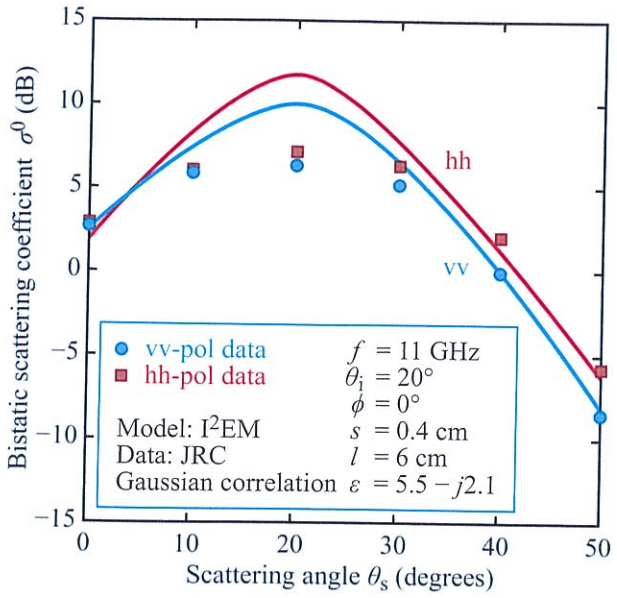

Figure 10-19: Comparison of I²EM-computed bistatic scattering coefficients with measurements as a function of the scattering angle θ_s.

correlation function, $s = 0.4$ cm and $l = 6$ cm. The surface was measured at 11 GHz and 13 GHz; only the 11 GHz data are shown in Fig. 10-19, as the 13 GHz data are almost identical, which is not surprising.

10-3.10 Applicability of Surface Scattering Models

Nature is far too complex for us to be able to describe it in terms of relatively simple models and mathematical functions. A natural random surface consists of multiple scales of roughness, so any description of its statistics in terms of a simple correlation function is certainly only an approximation, and even "direct" measurements of its rms height and correlation length are only estimates of its true statistical properties. The applicability of a model, be it theoretical or empirical, to a real surface is, at best, as good as the accuracies with which we know its statistics.

Models help us understand the observations made by our microwave sensors, and they guide our approach in the development of inversion techniques to estimate physical parameters—such as soil moisture content and surface roughness—from microwave observations.

10-4 Scattering by Random and Periodic Surfaces

As discussed in Section 5-12.5, for a monostatic radar, the coherent scattering component is important only over a narrow angular range of about 1° surrounding nadir incidence, and then only if the surface is relatively smooth ($ks \lesssim 0.5$). In this section, we examine the roles of surface roughness, and dielectric constant for periodic and nonperiodic surfaces.

10-4.1 Backscattering by Nonperiodic Random Surfaces

Surface roughness

We start by illustrating the angular variation of σ^0 for a statistically uniform surface of a dry asphalt parking lot. The measurements shown in Fig. 10-20 were conducted at 8.6 GHz, 17 GHz, and 35.6 GHz for hh, vv, and hv polarizations. The estimated value of the surface rms height is $s < 0.5$ cm. We note that:

(a) At all frequencies, the hh- and vv-polarized responses are essentially identical between normal incidence and $\theta \approx 10°$ and then they diverge as a function of θ, with σ^0_{vv} maintaining a higher level than σ^0_{hh}.

(b) The cross-polarized backscattering coefficient σ^0_{hv} exhibits a cosine-like angular dependence.

(c) Increasing the frequency from 8.6 GHz to 35.6 GHz is equivalent to increasing the electromagnetic roughness by a factor of 4. Increasing the roughness causes the angular plots of σ^0_{hh} and σ^0_{vv} to come closer together. Also, the level difference between σ^0_{hh} and σ^0_{hv} becomes narrower (more depolarization).

A similar set of measurements, conducted at the same frequencies and over the same angular range, are shown in Fig. 10-21 for a much rougher surface with an estimated rms height of 1.5 cm. The corresponding value of ks at 8.6 GHz is 2.7, which classifies the surface

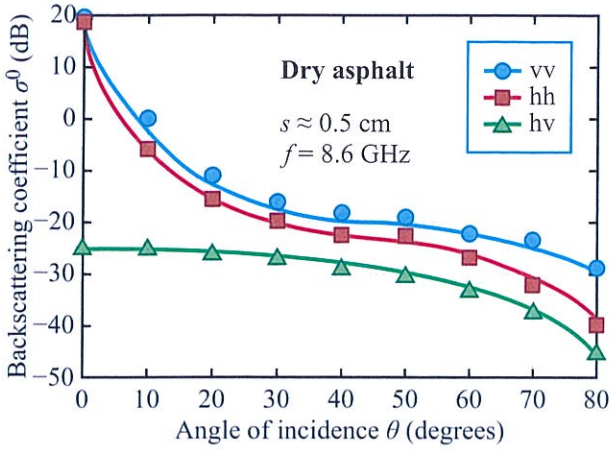

(a) 8.6 GHz

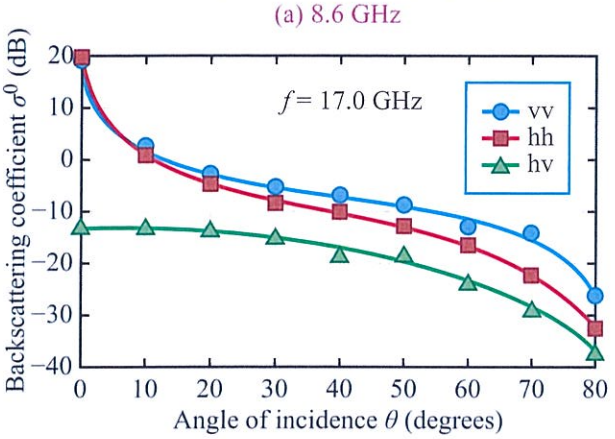

(b) 17.0 GHz

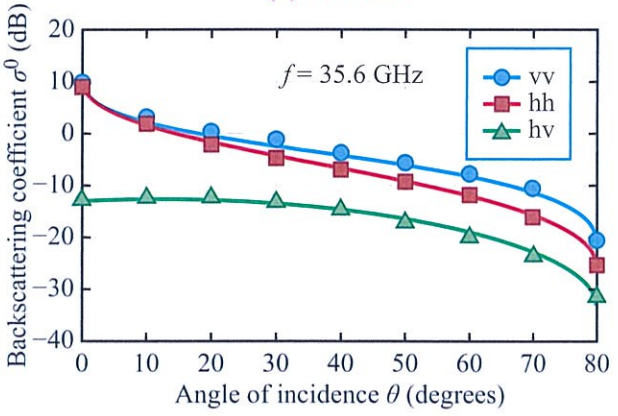

(c) 35.6 GHz

Figure 10-20: Measured backscattering coefficient of a dry asphalt surface at three microwave frequencies. The estimated value of the rms height is $s = 0.5$ cm.

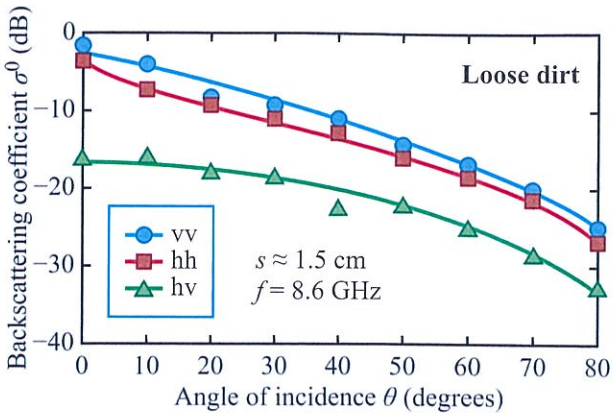

(a) 8.6 GHz

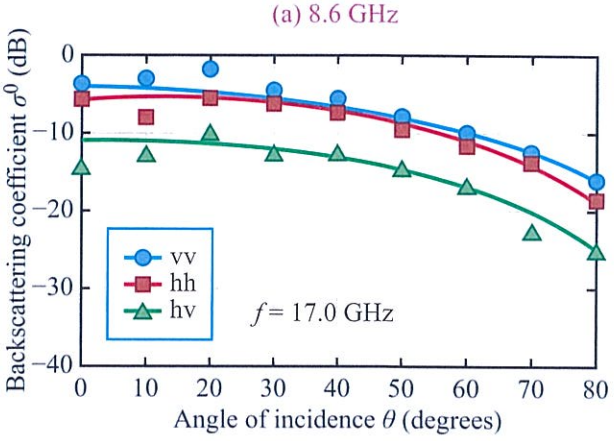

(b) 17.0 GHz

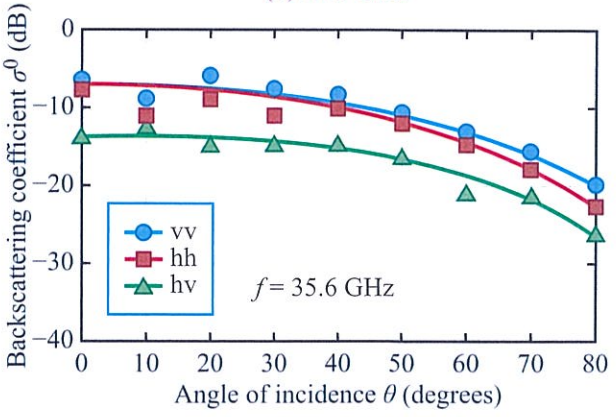

(c) 35.6 GHz

Figure 10-21: Measured backscattering coefficient of loose dirt with $s \approx 1.5$ cm at three microwave frequencies.

as electromagnetically very rough, and even more so at the higher frequencies. Consequently, (1) there is no evidence of the existence of a significant coherent component, (2) $\sigma^0_{hh} \approx \sigma^0_{vv}$ across the entire angular range, and (3) σ^0_{hv} is on the order of 5–10 dB below the level of the co-polarized backscattering coefficients.

Moisture content

Since (a) σ^0 is, to first order, proportional to the Fresnel reflectivity Γ, (b) Γ is dependent on the dielectric constant of a soil surface ε_{soil}, and (c) ε_{soil} is dependent on the volumetric moisture content m_v, it is not surprising that σ^0 also is soil moisture dependent. The data shown in Fig. 10-22 indicate that for a relatively smooth surface ($ks = 0.35$), σ^0 (in dB) increases approximately linearly with m_v at a rate of 0.24 dB/0.01 g/cm^3. In contrast, for the rough surface with $ks = 1.3$, the slope is 0.17 dB/0.01 g/cm^3. The data shown in Fig. 10-22 represent the early stage of a long investigation to develop a viable algorithm for estimating soil moisture content using an imaging radar system. The investigation culminated in the development of the inversion algorithm described in Section 10-5.

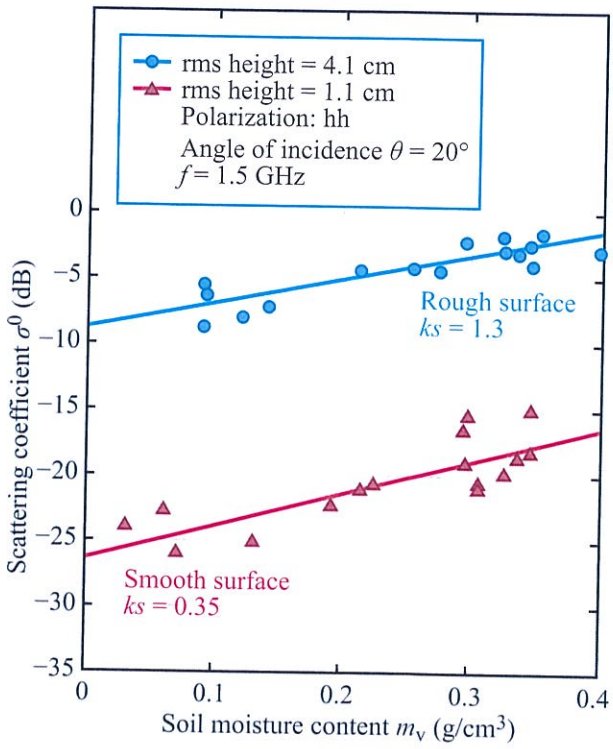

Figure 10-22: Measured 1.5 GHz response of σ^0_{hh} to m_v for a smooth surface with $ks = 0.35$ and a rougher surface with $ks = 1.3$ [from Ulaby et al., 1978].

10-4.2 Backscattering by Periodic Surfaces

Several types of agricultural crops are commonly planted in parallel rows, either in a rectangular format or in concentric rings (e.g., some types of center-pivot irrigated fields). In this subsection we examine the dependence of σ^0 on ***look direction***, where look direction is defined in terms of the azimuth angle ϕ_0 shown in Fig. 10-23, defined as the angle between the ground projection of the antenna beam axis and the x axis. The periodic variation is along the y direction, so $\phi_0 = 0$ is called the ***parallel look direction*** and $\phi_0 = 90°$ is called the ***perpendicular look direction***.

► One approach to calculating the backscattering coefficient of a composite surface is to assume that the scattering is caused exclusively by the random part of the surface and that the periodic component acts as a modulator of the local mean slope of the random surface component. ◄

A description of such a two-scale scattering model is given in Ulaby et al. (1982c). Another approach, which treats the random and periodic components together, was reported by Eom and Fung (1984).

Geometrical considerations

The sketch in Fig. 10-24(a) depicts a narrow-beam antenna pointed at a soil surface located in the x-y

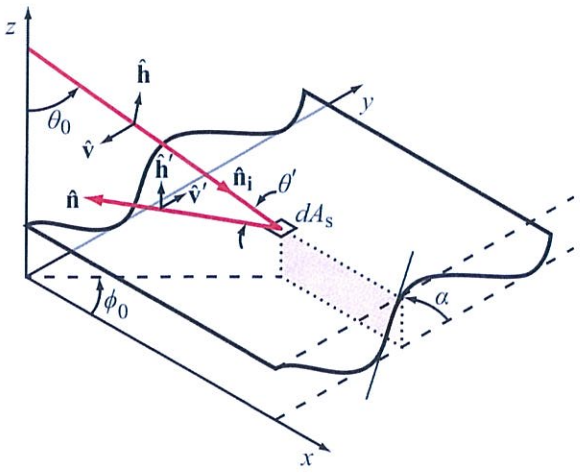

Figure 10-23: Parallel-look direction corresponds to $\phi_0 = 0$, and perpendicular-look direction corresponds to $\phi_0 = 90°$.

plane. The soil surface consists of ***random height variations*** denoted by $z(x,y)$ superimposed on a much larger, ***deterministic, one-dimensional periodic height variation*** denoted by

$$\mathcal{Z}(x,y) = \mathcal{Z}(y) = \mathcal{Z}(y+m\Lambda),$$

where m is any integer and Λ is the spatial period (row spacing) of the periodic pattern in the y direction. For a point (x,y) within the illuminated area in Fig. 10-24(a), the angle of incidence $\theta(x,y)$ is the angle between $-\hat{\mathbf{z}}$ and $\hat{\mathbf{n}}_i$, where $\hat{\mathbf{n}}_i$ is the unit vector in the propagation direction from the antenna to point (x,y).

Imaging radar

For an imaging radar, the resolution cell subtends an angular beamwidth so small that the angle of incidence θ is essentially constant for all points within the cell. This situation is depicted in Fig. 10-24(b). Furthermore, it is assumed that the dimensions of the cell are much larger than the spatial period Λ, so that many spatial cycles are included within the cell. (For simplicity of illustration, the resolution cell in Fig. 10-24(b) includes only part of one period). Recalling that the backscattering

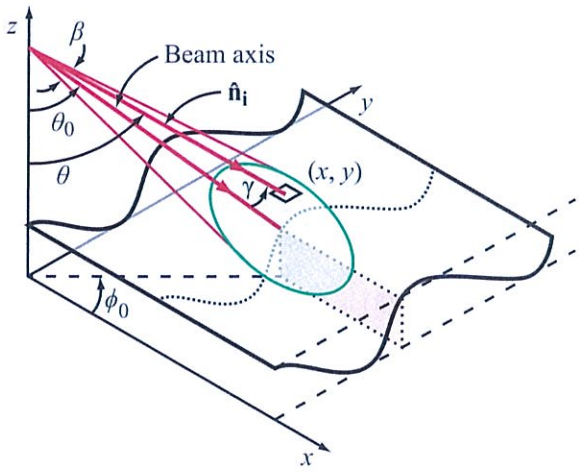

(a) Area observed by a pencil-beam scatterometer

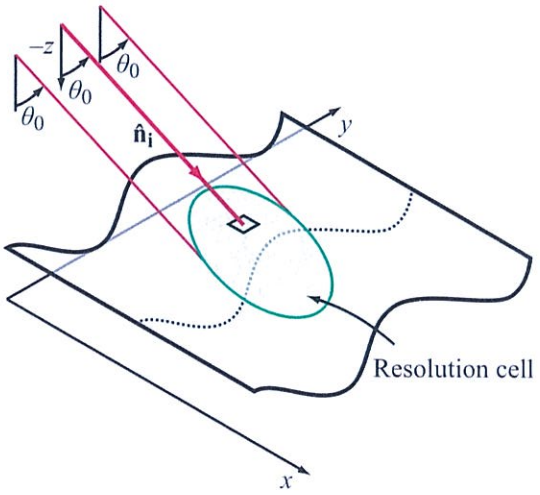

(b) Area observed by a high-resolution imager

Figure 10-24: Area as observed by (a) a pencil-beam scatterometer and (b) a high-resolution imager.

coefficient σ^0 of a resolution cell is equal to the radar cross section of the cell, σ, normalized by the physical cross-sectional area of the cell, A, the above assumption that the resolution cell contains many spatial periods leads to the conclusion that σ^0 may be determined by performing the calculation for a single rectangular strip within A whose dimensions are Λ in the y direction and some arbitrary length L_s in the x direction, with $L_s \gg l$,

where l is the correlation length of the random surface $z(x,y)$.

For a differential area $dx\,dy$ with center at (x,y) in the x-y plane, the corresponding area of the soil surface is given by

$$dA_s(x,y) = \left[\frac{dx}{\cos\alpha(y)}\right] dy, \tag{10.17}$$

where α (Fig. 10-23) is the angle whose tangent is equal to the slope of the periodic surface $\mathcal{Z}(y)$:

$$\tan\alpha(y) = \frac{d\mathcal{Z}(y)}{dy}. \tag{10.18}$$

For a linearly polarized antenna with a receive-transmit configuration denoted by pq, the ***observed backscattering coefficient*** $\sigma^0_{pq}(\theta_0,\phi_0)$ may be expressed as the incoherent integration over the rectangular strip

$$\sigma^0_{pq}(\theta_0,\phi_0) = \frac{\int_{y=0}^{\Lambda}\int_{x=0}^{L_s}\sigma^{ss}_{pq}(\theta')\,dA_s(x,y)}{\int_{y=0}^{\Lambda}\int_{x=0}^{L_s}dx\,dy}, \tag{10.19}$$

where $\sigma^{ss}_{pq}(\theta')$ is the backscattering coefficient of the differential area $dA_s(x,y)$, with the same polarization configuration as that of the radar antenna, and θ' is the local angle of incidence (Fig. 10-23). The superscript ss denotes the ***smaller-scale*** random roughness. The scattering by the differential area $dA_s(x,y)$ is governed by its surface characteristics and by the direction of the incident unit vector $\hat{\mathbf{n}}_i$ [Fig. 10-24(a)] relative to the local vector normal to the periodic surface $\hat{\mathbf{n}}$.

Upon inserting Eq. (10.17) into Eq. (10.19) and canceling out the dependence on x, Eq. (10.19) becomes

$$\sigma^0_{pq}(\theta_0,\phi_0) = \frac{1}{\Lambda}\int_0^{\Lambda}\sigma^{ss}_{pq}(\theta')\sec\alpha(y)\,dy. \tag{10.20}$$

Conical-beam scatterometer

For a circularly symmetric antenna beam with an antenna radiation pattern $F(\gamma)$, where γ is the angle away from the beam axis in Fig. 10-24(a), the variation in antenna gain across the illuminated cell may be accounted for by modifying Eq. (10.19) to

$$\sigma^0_{pq}(\theta_0,\phi_0) = \frac{\iint_{\text{main beam}} F^2(\gamma)\,\sigma^{ss}_{pq}(\theta')\sec\alpha(y)\,dx\,dy}{\iint_{\text{main beam}} F^2(\gamma)\,dx\,dy}. \tag{10.21}$$

Similar expressions may be derived for other antenna-beam configurations.

Sinusoidal periodic surface

To compute the integral given by Eq. (10.20), we need an expression for $\sigma^{ss}_{pq}(\theta')$ and the means to relate θ' and α to y. From the geometry in Fig. 10-23,

$$\theta' = \cos^{-1}(-\hat{\mathbf{n}}_i.\hat{\mathbf{n}}), \tag{10.22}$$

where unit vectors $\hat{\mathbf{n}}_i$ and $\hat{\mathbf{n}}$ are related to the incident direction (θ_0,ϕ_0) and the profile of the periodic surface as follows:

$$\hat{\mathbf{n}}_i = \hat{\mathbf{x}}\sin\theta_0\cos\phi_0 + \hat{\mathbf{y}}\sin\theta_0\sin\phi_0 - \hat{\mathbf{z}}\cos\theta_0, \tag{10.23}$$

$$\hat{\mathbf{n}} = (-\hat{\mathbf{x}}Z_x - \hat{\mathbf{y}}Z_y + \hat{\mathbf{z}})D_0, \tag{10.24}$$

where

$$D_0 = (1+Z_x^2+Z_y^2)^{-1/2},$$
$$Z_x = \frac{d\mathcal{Z}}{dx}, \qquad Z_y = \frac{d\mathcal{Z}}{dy}. \tag{10.25}$$

For a one-dimensional sinusoidal periodic surface that varies with y only, the periodic component is given by

$$\mathcal{Z}(y) = A\sin\left(\frac{2\pi y}{\Lambda}\right), \tag{10.26a}$$

and its slopes along x and y are

$$Z_x = \frac{d\mathcal{Z}}{dx} = 0, \tag{10.26b}$$

$$Z_y = \frac{d\mathcal{Z}}{dx} = \left(\frac{2\pi A}{\Lambda}\right)\cos\left(\frac{2\pi y}{\Lambda}\right), \tag{10.26c}$$

and

$$\alpha(y) = \tan^{-1}(Z_y). \tag{10.26d}$$

σ^0:	Averaged over one or more spatial periods, as would be observed by a radar
σ^s:	Small-scale roughness without periodic surface
σ^{ss}:	Small-scale roughness, modified by periodic surface

Small-scale random roughness $\sigma^{ss}_{pq}(\theta')$

Because of the periodic surface, the local coordinate system (x',y',z') of a differential area dA_s is, in general, different from the reference coordinate system (x,y,z). Consequently, the directions of the polarization vectors $\hat{\mathbf{h}}$ and $\hat{\mathbf{v}}$ in the reference (radar) coordinate system are not identical to $\hat{\mathbf{h}}'$ and $\hat{\mathbf{v}}'$ in the local coordinate system. To relate the two systems, we use the following relationships (from Ulaby et al., 1982a):

$$\hat{\mathbf{z}}' = \hat{\mathbf{n}}, \tag{10.27a}$$

$$\begin{aligned}\hat{\mathbf{y}}' = \frac{\hat{\mathbf{n}}\times\hat{\mathbf{n}}_i}{|\hat{\mathbf{n}}\times\hat{\mathbf{n}}_i|} &= D_1[\hat{\mathbf{x}}(Z_y\cos\theta_0 - \sin\theta_0\sin\phi_0)\\ &\quad + \hat{\mathbf{y}}(\sin\theta_0\cos\phi_0 - Z_x\cos\theta_0)\\ &\quad + \hat{\mathbf{z}}\sin\theta_0(Z_y\cos\phi_0 - Z_x\sin\phi_0)]\end{aligned} \tag{10.27b}$$

$$\begin{aligned}\hat{\mathbf{x}}' &= \hat{\mathbf{y}}'\times\hat{\mathbf{z}}'\\ &= \{\hat{\mathbf{x}}[\sin\theta_0\cos\phi_0 - Z_x\cos\theta_0\\ &\quad + \sin\theta_0(Z_y\cos\phi_0 - Z_x\sin\phi_0)Z_y]\\ &\quad + \hat{\mathbf{y}}[\sin\theta_0(Z_x\sin\phi_0 - Z_y\cos\phi_0)Z_x\\ &\quad + \sin\theta_0\sin\phi_0 - Z_y\cos\theta_0]\\ &\quad + \hat{\mathbf{z}}[(\sin\theta_0\sin\phi_0 - Z_y\cos\theta_0)Z_y\\ &\quad + (\sin\theta_0\cos\phi_0 - Z_x\cos\theta_0)Z_x]\}D_0D_1,\end{aligned} \tag{10.27c}$$

where

$$\begin{aligned}D_1 = \{&\sin^2\theta_0 + Z_x^2(\cos^2\theta_0 + \sin^2\theta_0\sin^2\phi_0)\\ &+ Z_y^2(\cos^2\theta_0 + \sin^2\theta_0\cos^2\phi_0)\\ &- 2\sin\theta_0\cos\theta_0(Z_x\cos\phi_0\\ &+ Z_y\sin\phi_0 + Z_xZ_y\tan\theta_0\sin\phi_0\cos\phi_0)\}^{-1/2}.\end{aligned} \tag{10.27d}$$

Note that the expressions given by Eq. (10.27) are for the general case where $Z_x \neq 0$. For a one-dimensional periodic surface with periodicity along the y direction, $Z_x = 0$.

The horizontal and vertical polarization vectors in the local and the reference frames are defined as follows:

$$\hat{\mathbf{h}}' = \hat{\mathbf{y}}', \tag{10.28a}$$

$$\hat{\mathbf{v}}' = -\hat{\mathbf{x}}'\cos\theta' - \hat{\mathbf{z}}'\cos\theta' \tag{10.28b}$$

$$\hat{\mathbf{h}} = -\hat{\mathbf{x}}\sin\phi_0 + \hat{\mathbf{y}}\cos\phi_0, \tag{10.28c}$$

$$\hat{\mathbf{v}} = -\hat{\mathbf{x}}\cos\theta_0\cos\phi_0 - \hat{\mathbf{y}}\cos\theta_0\sin\phi_0 - \hat{\mathbf{z}}\sin\theta_0. \tag{10.28d}$$

From Eq. (5.30), the backscattering coefficient $\sigma^0_{pq} = \sigma_{pq}/A$ is given by

$$\sigma^0_{pq} = \frac{4\pi R_r^2}{A}\frac{\mathcal{S}^s_p}{\mathcal{S}^i_q} = \frac{4\pi R_r^2}{A}\frac{|E^s_p|^2}{|E^i_q|^2} = \frac{4\pi}{A}|S_{pq}|^2, \tag{10.29}$$

where S_{pq} is the scattering amplitude of the target for incidence with polarization q and reception with polarization p. The derivation leading to the scattering coefficient of the random surface, $\sigma^{ss}_{pq}(\theta')$, encounters products of scattering amplitudes, necessitating the introduction of the generalized scattering coefficient

$$\sigma^0_{mnpq} = \frac{4\pi}{A}\,\mathfrak{Re}(S_{mn}S^*_{pq}). \tag{10.30}$$

In terms of this new definition and the polarization unit vectors defined by Eq. (10.28), the backscattering coefficients of the random surface are given by

$$\begin{aligned}\sigma^{ss}_{vv}(\theta') &= (\hat{\mathbf{v}}\cdot\hat{\mathbf{v}}')^4\,\sigma^s_{vv}(\theta') + (\hat{\mathbf{v}}\cdot\hat{\mathbf{h}}')^4\,\sigma^s_{hh}(\theta')\\ &\quad + 2(\hat{\mathbf{v}}\cdot\hat{\mathbf{h}}')^2(\hat{\mathbf{v}}\cdot\hat{\mathbf{v}}')^2\,\sigma^s_{vvhh}(\theta'),\end{aligned} \tag{10.31a}$$

$$\begin{aligned}\sigma^{ss}_{hh}(\theta') &= (\hat{\mathbf{h}}\cdot\hat{\mathbf{v}}')^4\,\sigma^s_{vv}(\theta') + (\hat{\mathbf{h}}\cdot\hat{\mathbf{h}}')^4\,\sigma^s_{hh}(\theta')\\ &\quad + 2(\hat{\mathbf{h}}\cdot\hat{\mathbf{h}}')^2(\hat{\mathbf{h}}\cdot\hat{\mathbf{v}}')^2\,\sigma^s_{vvhh}(\theta'),\end{aligned} \tag{10.31b}$$

and

$$\begin{aligned}\sigma^{ss}_{vh}(\theta') &= (\hat{\mathbf{v}}\cdot\hat{\mathbf{v}}')^2(\hat{\mathbf{v}}'\cdot\hat{\mathbf{h}})^2\,\sigma^s_{vv}(\theta')\\ &\quad + (\hat{\mathbf{v}}\cdot\hat{\mathbf{h}}')^2(\hat{\mathbf{h}}'\cdot\hat{\mathbf{h}})^2\,\sigma^2_{hh}(\theta')\\ &\quad + 2(\hat{\mathbf{v}}\cdot\hat{\mathbf{v}}')(\hat{\mathbf{v}}'\cdot\hat{\mathbf{h}})(\hat{\mathbf{v}}\cdot\hat{\mathbf{h}}')(\hat{\mathbf{h}}'\cdot\hat{\mathbf{h}})\,\sigma^s_{vvhh}(\theta')\\ &\quad + [(\hat{\mathbf{v}}\cdot\hat{\mathbf{v}}')(\hat{\mathbf{h}}'\cdot\hat{\mathbf{h}}) + (\hat{\mathbf{v}}\cdot\hat{\mathbf{h}}')(\hat{\mathbf{v}}'\cdot\hat{\mathbf{h}})]^2\,\sigma^s_{hv}(\theta').\end{aligned} \tag{10.31c}$$

Here, σ_{vv}^{ss} is the vv-polarized coefficient of the smaller-scale roughness, defined in the antenna coordinate system, whereas σ_{vv}^{s} is the vv-polarized backscattering coefficient of the same random surface, but without the periodic surface. An examination of Eq. (10.31a) shows that the dominant term is $(\hat{\mathbf{v}} \cdot \hat{\mathbf{v}}')^4 \, \sigma_{vv}^{s}(\theta')$. Similarly, the dominant term in Eq. (10.31b) is $(\hat{\mathbf{h}} \cdot \hat{\mathbf{h}}')^4 \, \sigma_{hh}^{s}(\theta')$. In Eq. (10.31c), the first three terms tend to cancel and the last term is representative of $\sigma_{vh}^{ss}(\theta')$.

Model behavior

Before we examine the dependence of the backscattering coefficient of a periodic surface on the parameters of that surface, let us review the results obtained so far. Equation (10.20) expresses the backscattering coefficient $\sigma_{pq}^{0}(\theta_0, \phi_0)$, as observed by an imaging radar illuminating the periodic surface at an angle of incidence θ_0 (measured relative to the mean surface) and an azimuth angle ϕ_0, in terms of a line integral involving $\sigma_{pq}^{ss}(\theta')$, which is the backscattering coefficient of a differential area whose surface normal is at an angle θ' relative to the observation direction. The integral is an incoherent summation of backscattering contributions from all elemental areas observed by the radar over one spatial period Λ.

An incident wave with a linear (horizontal or vertical) polarization orientation (as defined in the antenna reference frame) generally has both $\hat{\mathbf{h}}$ and $\hat{\mathbf{v}}$ components in the local coordinate system of the differential area dA_s. Consequently, the backscattering coefficient $\sigma_{hh}^{ss}(\theta')$ of the area dA_s is not only related to $\sigma_{hh}^{s}(\theta')$, the backscattering coefficient of dA_s in its own coordinate system, but also includes contributions related to the backscattering coefficients $\sigma_{vv}^{s}(\theta')$ and $\sigma_{vvhh}^{s}(\theta')$ of the area.

The backscattering coefficients having the single s superscript characterize the backscattering properties of the random surface in the absence of the periodic surface. To illustrate the effect of the periodic surface and look angle on the hh-backscattering coefficient, we apply the model to two surfaces with identical sinusoidal surfaces, but with very different random components. The angular plot of the backscattering coefficient of the random component $\sigma_{hh}^{s}(\theta')$ is displayed in Fig. 10-25

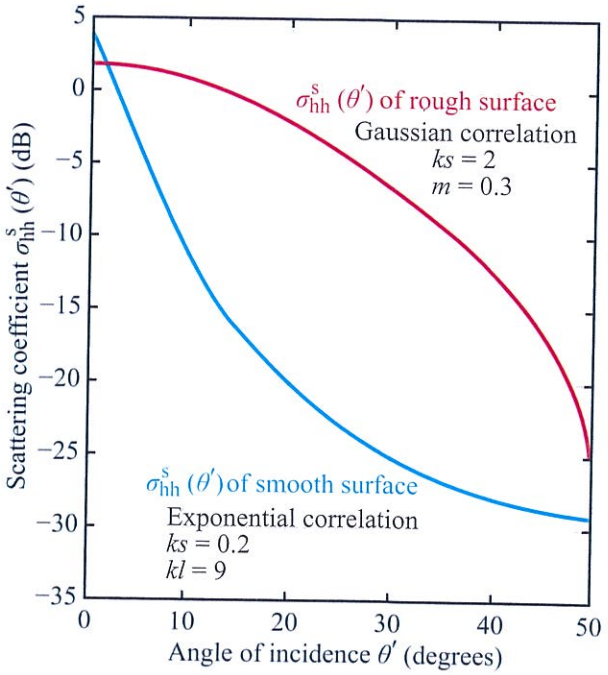

Figure 10-25: Angular plots of $\sigma_{hh}^{s}(\theta')$ for smooth and rough random surfaces in the absence of the periodic surface.

for both surfaces. The smooth random surface, which is characterized by a roughness $ks = 0.2$, exhibits an angular variation of 28 dB between $\theta' = 0$ and $\theta' = 30°$. In contrast, the rough surface with $ks \approx 2$ exhibits a much smaller angular variation of only 10 dB over the same angular range.

As stated earlier in connection with the expression for $\sigma_{hh}^{ss}(\theta')$ given by Eq. (10.31b), the dominant term is the second term. That is,

$$\sigma_{hh}^{ss}(\theta') \approx (\hat{\mathbf{h}} \cdot \hat{\mathbf{h}}')^4 \, \sigma_{hh}^{s}(\theta').$$

Computing $\sigma_{hh}^{0}(\theta_0, \phi_0)$ at incidence angle θ_0 and azimuth look-angle ϕ_0 entails performing the integration in Eq. (10.20). For each value of the integration variable y, (1) Eq. (10.26) provides values for Z_x, Z_y, and α, which then (2) specify $\hat{\mathbf{n}}_i$ and $\hat{\mathbf{n}}$, which in turn specify θ' by Eq. (10.22). Also, use of Eqs. (10.27) and (10.28) specifies $\hat{\mathbf{h}}$ and $\hat{\mathbf{h}}'$.

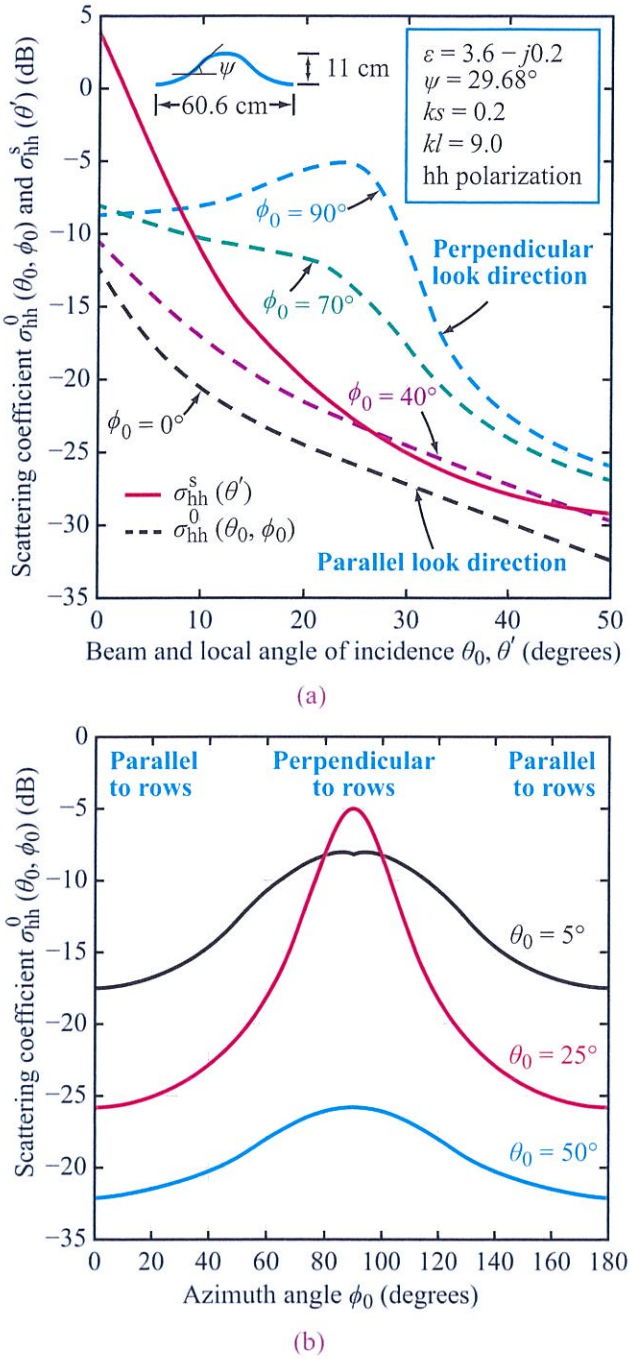

Figure 10-26: Periodic surface with relatively smooth random undulations. (a) Variation of the scattering coefficient $\sigma^0_{hh}(\theta_0, \phi_0)$ as a function of the beam angle of incidence θ_0 for several values of the azimuth angle ϕ_0, and (b) variation of $\sigma^0_{hh}(\theta_0, \phi_0)$ with the azimuth angle ϕ_0.

Figure 10-26(a) displays plots for $\sigma^0_{hh}(\theta_0, \phi_0)$ as a function of θ_0 for specific values of ϕ_0, and Fig. 10-26(b) displays plots as a function of ϕ_0 at specific values of θ_0, all for a smooth random surface with $ks = 0.2$. The periodic surface is sinusoidal with an amplitude $A = 5.5$ cm and a spatial period $\Lambda = 60.6$ cm. The greatest contrast is between $\phi_0 = 0$ (parallel look direction) and $\phi_0 = 90°$ (perpendicular look direction). At $\theta_0 = 25°$, the variation of $\sigma^0_{hh}(\theta_0, \phi_0)$ with ϕ_0 exceeds 20 dB!

Similar plots are shown in Fig. 10-27 for a surface with the same periodic structure, but with a much rougher random-surface component. Not surprisingly, $\sigma^0_{hh}(\theta_0, \phi_0)$ is much less sensitive to look direction.

Experimental observations

Variations in σ^0 due to look direction have been observed by scatterometers (Batlivala and Ulaby, 1976; Ulaby and Bare, 1979; Bradley and Ulaby, 1981; Fenner et al., 1981; Ulaby et al., 1982c) and registered on radar imagery (Batlivala and Ulaby, 1976; MacDonald and Waite, 1978; Blanchard and Chang, 1983). An example is shown in Fig. 10-28, which displays plots of σ^0 versus time as measured by airborne scatterometers passing over a rectangular wheat-stubble field with row configurations as illustrated. The presence of wheat stubble above the soil surface has almost no discernible effect on the backscattering behavior of the soil background. Hence, for all practical purposes, at microwave frequencies a wheat-stubble field may be regarded as a bare soil surface. Over the triangular sections at each end of the field, the radar look direction is orthogonal to row direction ($\phi_0 = 90°$), whereas over the middle section of the field, the radar look direction is parallel to row direction ($\phi_0 = 0°$). The plots shown are for observations at $\theta_0 = 20°$ and include like-polarized (hh and vv) plots at 1.6, 4.75, and 13.3 GHz and hv-polarized plots at 1.6 and 4.75 GHz. For the like-polarized plots, the change in the level of σ^0 across the boundary between $\phi_0 = 0°$ and $\phi_0 = 90°$ is largest at 1.6 GHz and smallest at 13.3 GHz. This behavior is predictable, because the random roughness component becomes increasingly rough as the frequency increases. A rougher random surface exhibits a σ^s versus θ' curve

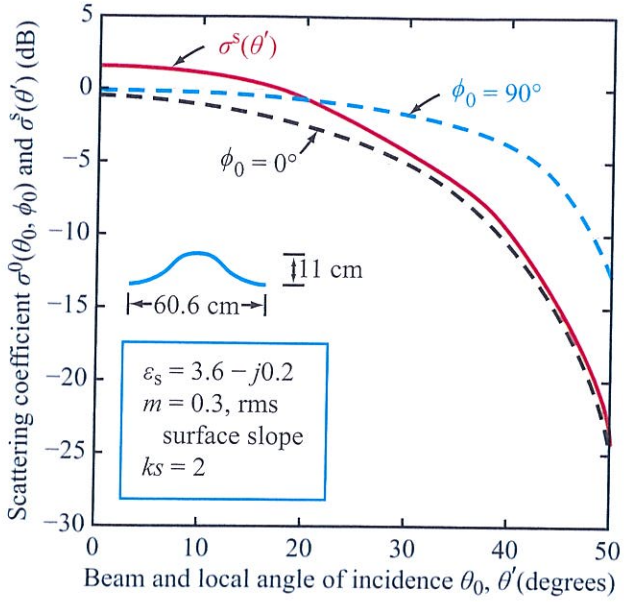

(a)

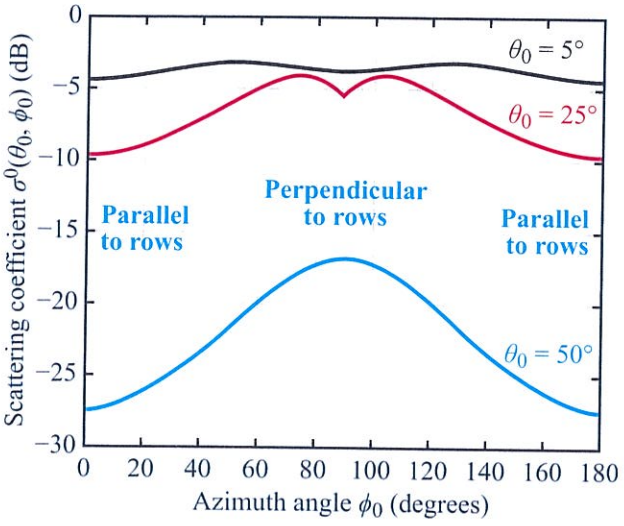

(b)

Figure 10-27: Periodic surface with rough random undulations. (a) Variation of the scattering coefficient $\sigma^0_{hh}(\theta_0, \phi_0)$ as a function of the beam angle of incidence θ_0 for several values of the azimuth angle ϕ_0, and (b) variation of $\sigma^0_{hh}(\theta_0, \phi_0)$ with the azimuth angle ϕ_0.

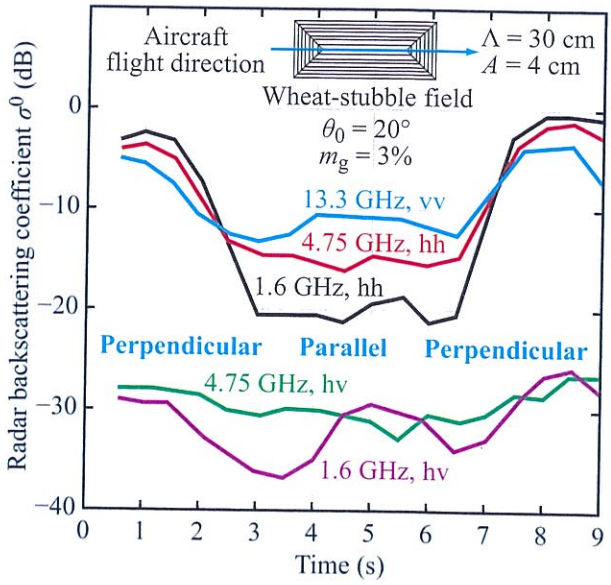

Figure 10-28: Scatterometer time response for a wheat-stubble field [Ulaby et al., 1982c].

with a slower decay rate, which results in reduced sensitivity to look direction.

► In contrast to the like-polarization scattering coefficient, the cross-polarization scattering coefficient shows a much weaker sensitivity to row direction. ◄

Information about the cross-polarization isolation performance of the antennas suggests that part of the observed increase in σ^0_{hv} across the boundaries between the $\phi = 0°$ and $\phi = 90°$ regions is actually due to the coupling of part of the like-polarized return to the cross-polarized receiving antenna. Thus, the actual sensitivity of σ^0_{hv} to row direction may be even weaker than indicated in Fig. 10-28. Based on theoretical considerations, σ^0_{hv} should indeed exhibit a very weak dependence on ϕ_0 because, as noted in connection with Figs. 10-20 and 10-21, σ^s_{hv} is weakly dependent on incidence angle, particularly in the region between $\theta' = 0°$ and 40°.

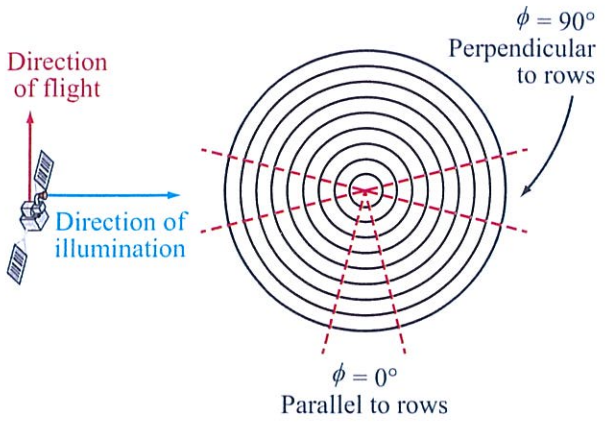

(a) Illumination geometry

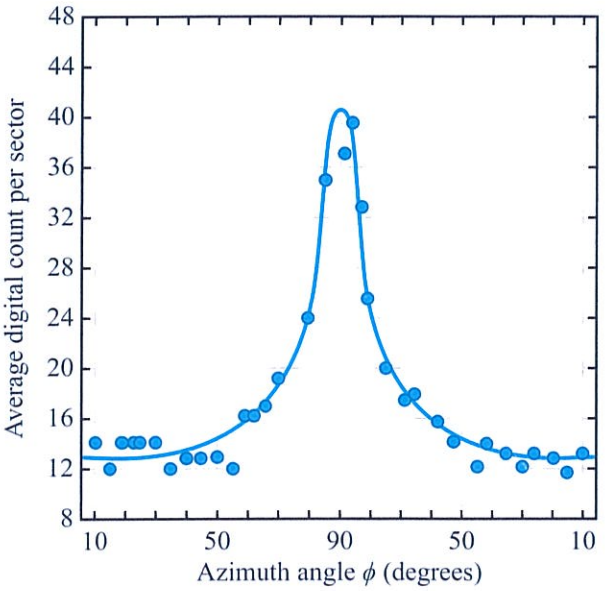

(b) Measured data

Figure 10-29: Graphic illustration of the difference between Seasat SAR returns as influenced by tillage direction [from Blanchard and Chang, 1983].

Figure 10-29(a) shows the geometry associated with the radar observation of a circularly tilled field. Assuming that the radar platform is moving northward and the radar beam is pointing eastward, the narrow biconical section of the field (whose axis is east-west) contains rows that are approximately orthogonal to the radar look direction ($\phi_0 = 90°$). The plot in Fig. 10-29(b) displays the variation in image intensity, averaged along radial vectors originating at the center of the field, as a function of the azimuth angle ϕ_0 for a field with a circularly tilled surface (Blanchard and Chang, 1983). The data, which were obtained from a digital Seasat-A SAR image of the field, show that the backscattered power (which is proportional to σ^0) is highest for pixels corresponding to $\phi_0 \approx 90°$ and lowest for those corresponding to $\phi_0 \approx 0°$. These results are in good agreement with the theoretical plots shown in Fig. 10-26.

10-5 PRISM (Polarimetric Radar Inversion for Soil Moisture)

Both theoretical models and experimental observations indicate that for a random surface observed by a radar at an incidence angle θ and microwave frequency f:

(a) The magnitudes of the surface backscattering coefficients σ^0_{vv}, σ^0_{hh}, and σ^0_{hv} are governed primarily by the rms height s and moisture content m_v, and secondarily by the correlation length l.

(b) At incidence away from nadir, the co-pol ratio $p = \sigma^0_{hh}/\sigma^0_{vv}$ of a relatively smooth surface (with $ks \approx 0.1$) is on the order of 0.1 to 0.4 (depending on θ and m_v), and increases with ks to 1 as ks increases to beyond 2.

(c) For a perfectly smooth surface, $\sigma^0_{hv} = 0$. Increasing surface roughness causes the cross-pol ratio $q = \sigma^0_{hv}/\sigma^0_{vv}$ to increase monotonically with ks, reaching a plateau as ks exceeds 2.

These considerations suggest that it should be possible to retrieve the values of s and m_v of a random surface from the measurement of the three scattering coefficients. To develop such a model, a University of Michigan team conducted field experiments using a mobile, truck-mounted, multifrequency, polarimetric scatterometer, supported by a laser-profiling system to measure the height profiles of the observed surfaces and a microwave dielectric probe to measure the dielectric constant and moisture content of the soil medium (Oh et al., 1992). The study included four surfaces with roughnesses extending from $s = 0.32$ cm

to $s = 3.02$ cm, each observed under dry and wet soil conditions. The objective of the study was not only to quantify the radar backscatter response to surface roughness and soil moisture content, but also to develop a semiempirical inversion model to estimate surface roughness and soil moisture content from multipolarized radar observations. The inversion algorithm that emerged from the 1992 study—which we call the ***Polarimetric Radar Inversion for Soil Moisture-1***, or ***PRISM-1*** for short—is discussed in Section 10-5.2. A few years later, additional experiments were conducted using a variety of radar instruments including airborne polarimetric SARs, which led to a slightly modified version of PRISM-1, which we refer to as ***PRISM-2***. Its details are covered in Section 10-5.3.

10-5.1 Co-Pol and Cross-Pol Ratios

As a prelude to developing an inversion model, it is important to analyze the behavior of σ^0 as a function of θ, ks, m_v, and f.

The role of roughness is evident by comparing the experimental data displayed in Fig. 10-30(a) for a smooth surface (with $s = 0.32$ cm) at 1.5 GHz ($ks = 0.1$) with those in Fig. 10-30(b) for a rough surface (with $s = 3.02$ cm) at 9.5 GHz ($ks = 6$). The volumetric moisture contents of the two surfaces are essentially the same (0.14 for the smooth surface and 0.16 for the rough surface). The co-polarized backscattering coefficients ($\sigma^0_{hh}(\theta)$ and $\sigma^0_{vv}(\theta)$) of the smooth surface exhibit steep angular responses (≈ 45 dB drop between $\theta = 10°$ and $\theta = 70°$), compared with much gentler responses for the rough surface (≈ 12 dB drop between $\theta = 10°$ and $\theta = 70°$). The over 30 dB difference in the angular slope translates to a factor of over 1000 in m^2/m^2. That is, the angular decay rate, on average, is about 1000 times greater for the smooth surface [Fig. 10-30(a)] than for the rough surface [Fig. 10-30(b)].

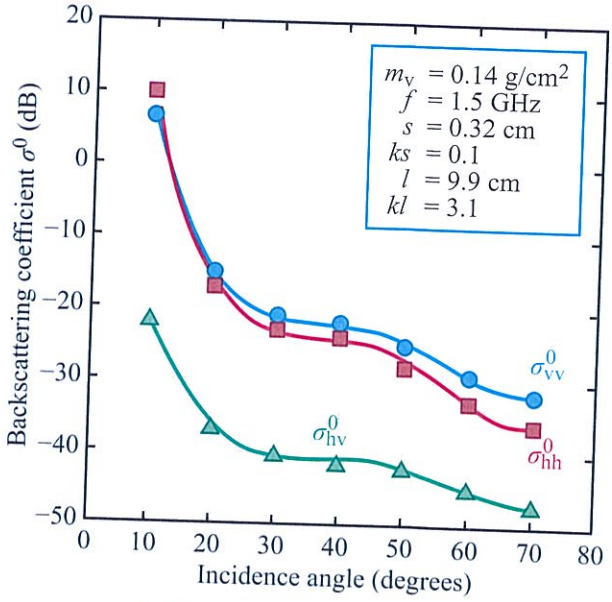

(a) Smooth surface at 1.5 GHz

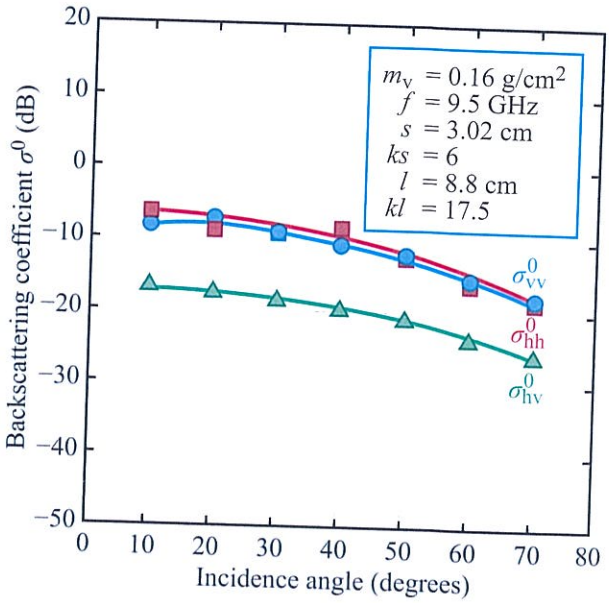

(b) Very rough surface at 9.5 GHz

Figure 10-30: Measured backscattering coefficient of (a) a smooth surface with $s = 0.32$ cm at 1.5 GHz and (b) a rough surface with $s = 3.02$ cm at 9.5 GHz.

Co-polarized ratio

Based on the data in Fig. 10-30 and other data reported by Oh et al. (1992), the ***co-polarized ratio***, defined as

$$p = \frac{\sigma^0_{hh}}{\sigma^0_{vv}}, \tag{10.32}$$

is observed to always be smaller than or equal to 1, and it approaches 1 as ks becomes large. In dB,

$$p(\text{dB}) = \sigma^0_{hh}(\text{dB}) - \sigma^0_{vv}(\text{dB}), \tag{10.33}$$

which in Fig. 10-30 is the difference between the levels of σ^0_{hh}(dB) and σ^0_{vv}(dB). The measured variation of p(dB) with ks is shown in Fig. 10-31 for dry and wet soil surfaces observed at $\theta = 50°$. We observe that p depends on both ks and ε, but it approaches 0 dB and becomes essentially independent of the dielectric constant ε for $ks \geq 2$.

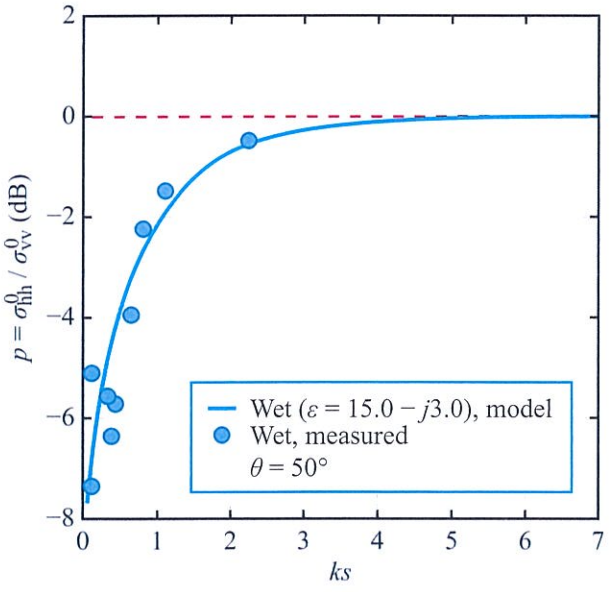

Figure 10-31: Measured and modeled variation of the co-pol ratio p with EM roughness ks.

Oh et al. (1992) developed the following empirical model† for the co-polarized ratio p:

$$p = \frac{\sigma^0_{hh}}{\sigma^0_{vv}} = \left[1 - \left(\frac{2\theta}{\pi}\right)^{\alpha} e^{-ks}\right]^2, \tag{10.34}$$

where θ is the incidence angle in radians, $k = 2\pi/\lambda$, s is the rms height, and

$$\alpha = \frac{1}{3\Gamma_0}, \tag{10.35}$$

with Γ_0 representing the surface (Fresnel) reflectivity at normal incidence,

$$\Gamma_0 = \left|\frac{1-\sqrt{\varepsilon}}{1+\sqrt{\varepsilon}}\right|^2. \tag{10.36}$$

As noted in Section 4-8, the dielectric constant ε of the soil surface is strongly dependent on the volumetric moisture content m_v.

Cross-polarized ratio

The ***cross-polarized ratio***, defined as

$$q = \frac{\sigma^0_{hv}}{\sigma^0_{vv}}, \tag{10.37}$$

exhibits a strong dependence on ks, as shown in Fig. 10-32, and can be modeled empirically as

$$q = 0.23\Gamma_0^{1/2}[1 - e^{-ks}]. \tag{10.38}$$

Using the empirical models developed for p and q, the following models were developed for σ^0_{vv}, σ^0_{hh}, and σ^0_{hv}:

$$\sigma^0_{vv} = 0.7\left[1 - e^{-0.65(ks)^{1.8}}\right]\frac{\cos^3\theta}{\sqrt{p}}[\Gamma_v(\theta) + \Gamma_h(\theta)], \tag{10.39a}$$

$$\sigma^0_{hh} = p\sigma^0_{vv}, \tag{10.39b}$$

$$\sigma^0_{hv} = q\sigma^0_{vv}. \tag{10.39c}$$

† **Computer Code 10.5.**

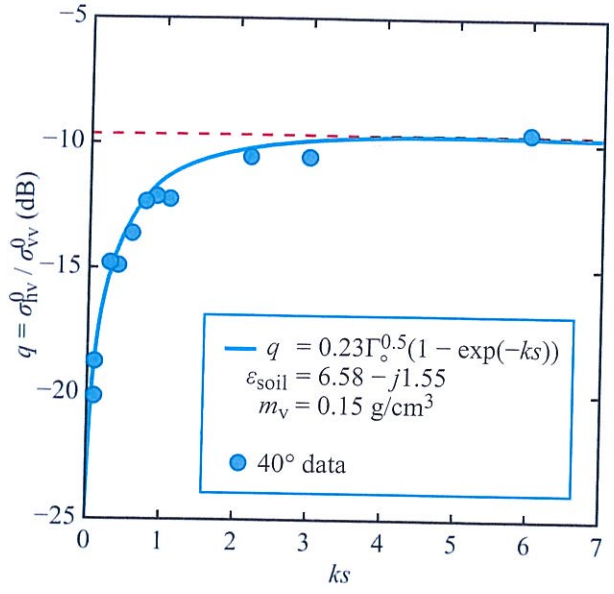

(a) Dry soil

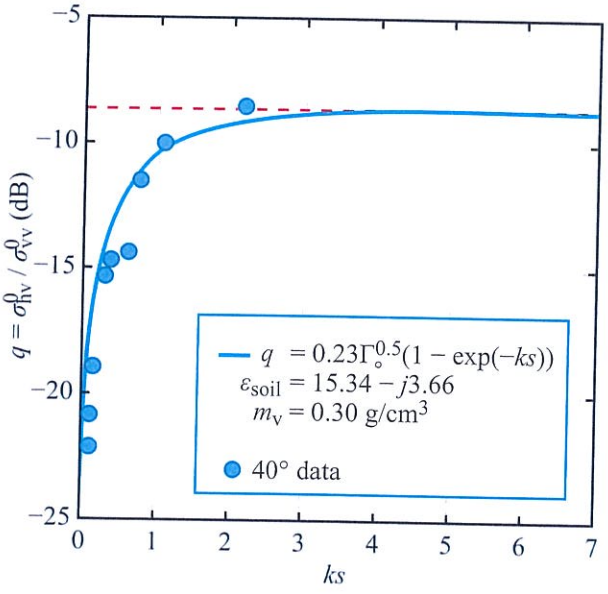

(b) Wet soil

Figure 10-32: Measured and modeled variation of the cross-pol ratio q with EM roughness ks for (a) a dry and (b) a wet soil surface [Oh et al., 1992].

The expressions given by Eqs. (10.34) to (10.39) constitute the ***forward model*** of PRISM-1.

10-5.2 PRISM-1

Using the models for p and q, a nonlinear inversion model (PRISM-1) was developed to estimate the values of ks, ε', ε'', and m_v. An example is shown in Fig. 10-33 for $f = 1.25$ GHz and $\theta = 30°$. The combination of p and q provides values for s and m_v. Comparisons between estimated values and measured values are provided in Fig. 10-34. The rms error for m_v is 0.04 g/cm^3, which is as good as the rms error associated with measuring m_v directly under field conditions. To measure m_v for an area extensive target, several soil samples are acquired from different spatial locations and processed to determine their mean value and associated standard deviation. Even under very uniform soil conditions, the spatial variability alone (i.e.,

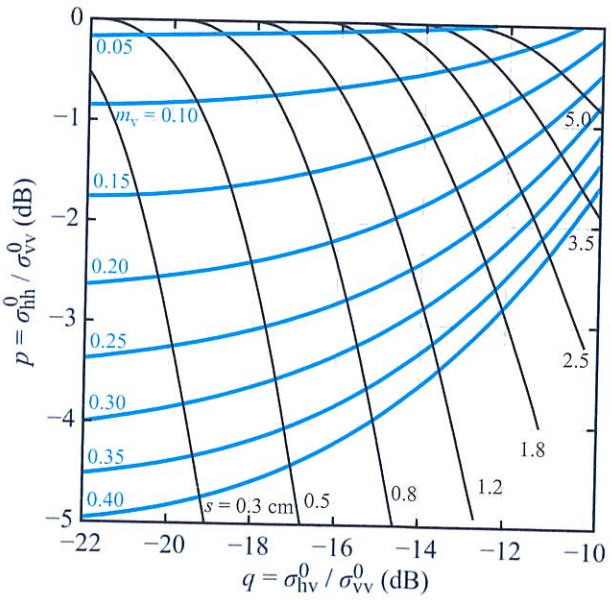

Figure 10-33: PRISM-1 uses the co-pol ratio p and cross-pol ratio q at any specified frequency/angle combination to estimate the values of the rms height s and volumetric moisture m_v. This algorithm is for $f = 1.25$ GHz and $\theta = 30°$.

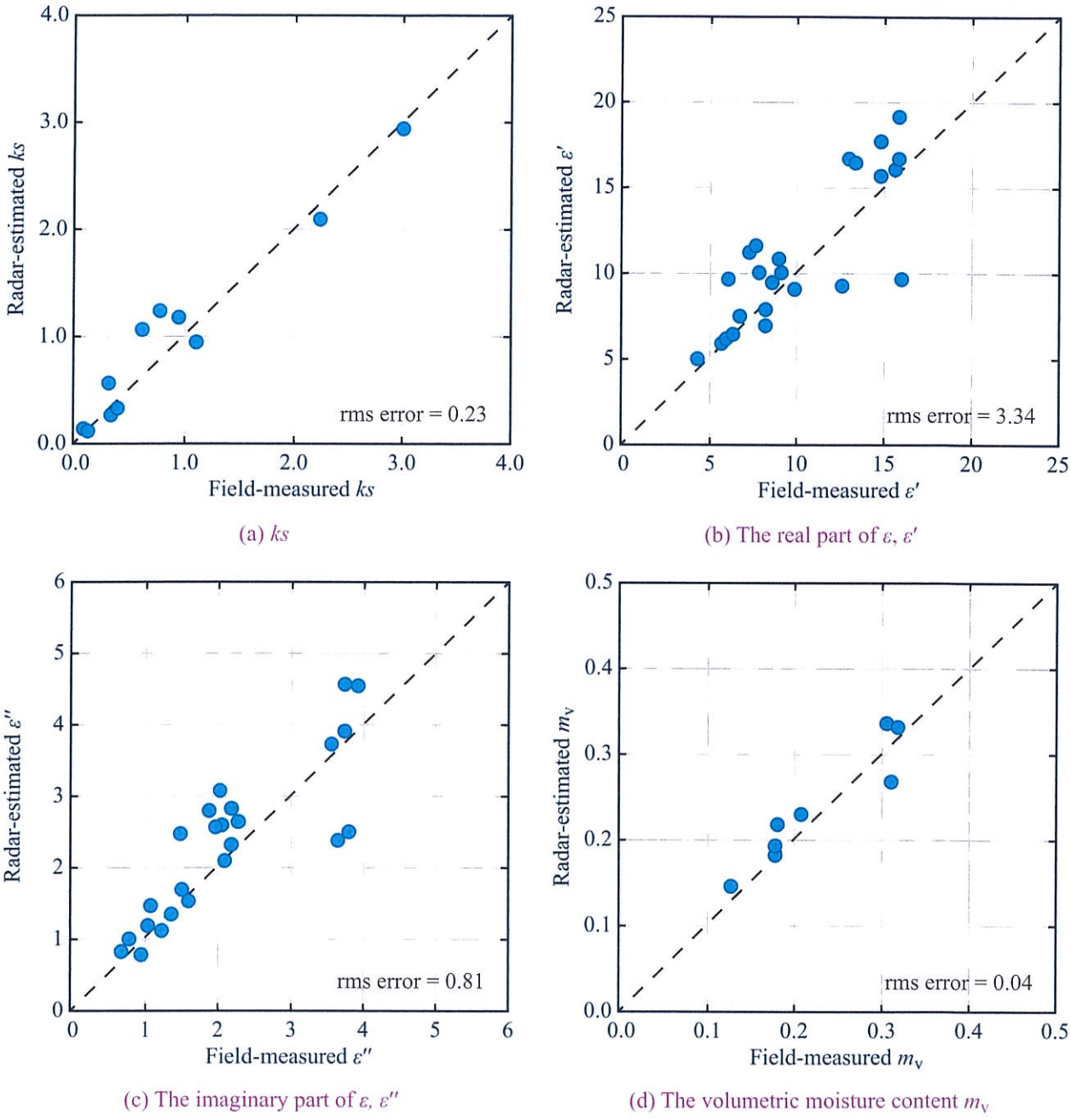

(a) *ks*

(b) The real part of ε, ε'

(c) The imaginary part of ε, ε''

(d) The volumetric moisture content m_v

Figure 10-34: Comparison of radar-estimated values (based on PRISM-1) of *ks*, ε', ε'', and m_v with corresponding values measured directly [Oh et al., 1992].

ignoring measurement error of the dielectric probe used to measure m_v) is on the order of 0.04 g/cm^3. This means that the precision associated with the values estimated by the radar is comparable to the natural spatial variability of m_v.

10-5.3 PRISM-2

Even though the 1992 empirical model for σ^0 provides very good fits to the measured data and the inverse model provides accurate soil moisture estimates, we should keep in mind that the project represents a single experiment involving only four different soil surfaces. Over the next decade, many more experiments were conducted, using not only truck-mounted and indoor scatterometers, but also several flights by the JPL AirSAR over test sites in Michigan, Oklahoma, and California. The combined data set of the seven experiments encompassed approximately 40 bare soil fields, with ks values extending over the range from 0.13 to 6.98 and volumetric moisture values covering the range from 0.04 to 0.29 g/cm^3 (Oh et al., 2002).

Using the expanded data set, a new semiempirical model was developed (PRISM-2), but this time m_v was used explicitly as an independent variable, rather than through ε and Γ as was done previously in the model given by Eqs. (10.34), (10.38), and (10.39). The 2004 model (Oh, 2004) takes the form

$$\sigma^0_{vh} = 0.11 m_v^{0.7} (\cos\theta)^{2.2} \left[1 - e^{-0.32(ks)^{1.8}}\right], \quad (10.40a)$$

$$p = \frac{\sigma^0_{hh}}{\sigma^0_{vv}} = 1 - \left(\frac{2\theta}{\pi}\right)^{0.35 m_v^{-0.65}} \cdot e^{-0.4(ks)^{1.4}}, \quad (10.40b)$$

$$q = \frac{\sigma^0_{hv}}{\sigma^0_{vv}} = 0.095(0.13 + \sin 1.5\theta)^{1.4} \left[1 - e^{-1.3(ks)^{0.9}}\right]. \quad (10.40c)$$

In this model, the cross-polarized ratio q is a function of only θ and ks. Its variation with ks is shown in Fig. 10-35(a) for $\theta = 45°$. Parts (b) and (c) depict the variations of σ^0_{vh} and p with m_v and ks.

Using the model expressions of Eq. (10.40), Oh (2004) developed an inverse model to generate estimates of ks and m_v from the multipolarized radar measurements. Figure 10-36 compares field-measured values

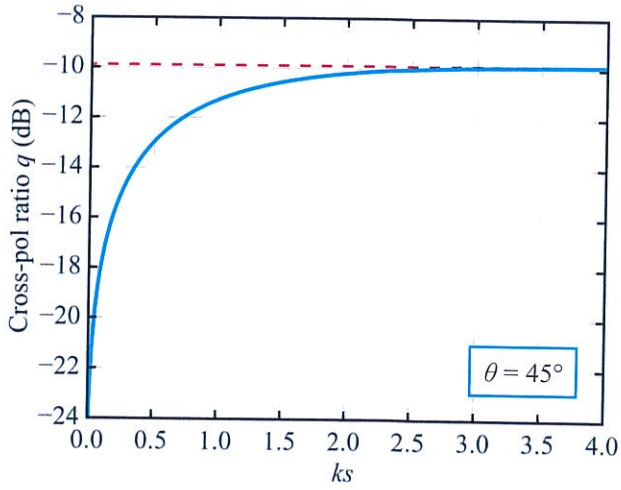

(a) q versus ks

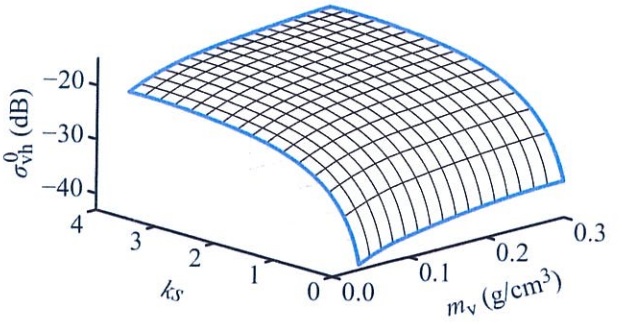

(b) Mesh plot of σ^0_{vh} against ks and m_v

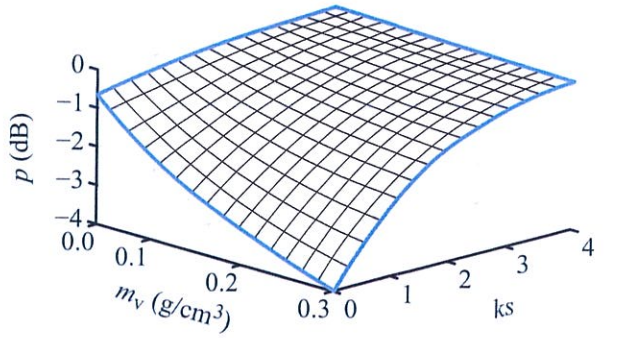

(c) Mesh plot of p against m_v and ks

Figure 10-35: PRISM-2 plots of (a) the cross-pol ratio q as a function of ks at $\theta = 45°$, (b) σ^0_{hv}, and (c) co-pol ratio p.

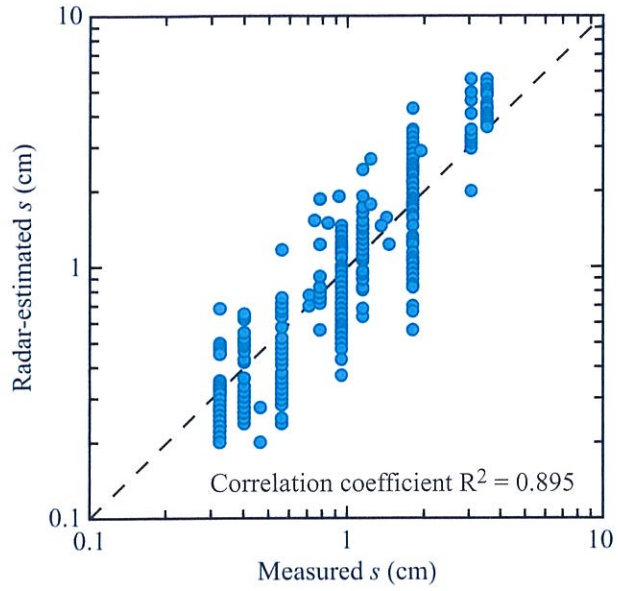

(a) rms height s

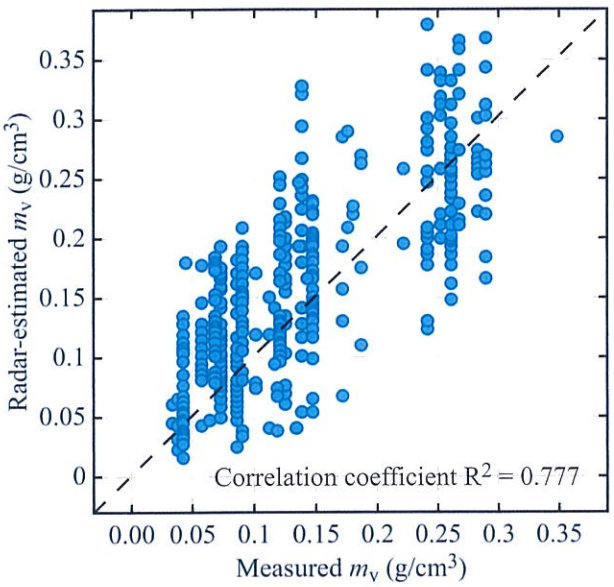

(b) Volumetric moisture content m_v

Figure 10-36: Comparison of radar-estimated values of s and m_v using PRISM-2 with corresponding values measured directly. Each data point represents a single frequency/angle combination [Oh, 2004].

of s and m_v with values estimated using the inverse model applied to 414 data vectors composed of σ^0_{hh}, σ^0_{hv}, and σ^0_{vv} at 1 angle $\times$ 1 frequency $\times$ 1 soil-surface condition. For each field-measured value of ks or m_v, multiple estimated values are generated by the inverse model—corresponding to the various frequency/angle combinations of available radar observations. Part of the variability along the vertical axes in Figs. 10-36(a) and (b) is due to the imprecision of the inversion model, but some of the variability is due to intercalibration among the various radars and field campaigns. When the multiple estimates of ks generated from the multiple frequency/angle combinations are averaged together, much of the variability disappears. The result is shown in Fig. 10-37.

In addition to the I^{2}EM theoretical model described in Section 10-3 and the empirical models presented in the present section, the literature contains other theoretical and empirical models for radar scattering by random surfaces, two of which are presented in forthcoming sections. Intercomparison of some of the available models was performed by Baghdadi et al. (2011). Also, concerted efforts have been devoted to advancing the development of soil moisture inversion algorithms that incorporate simultaneous radar and radiometer observations (Njoku et al., 2002; Narayan et al., 2006; Zhan et al., 2006). A major challenge faced by such an approach is the large difference in the spatial-resolution capabilities of the two sensors: tens of kilometers for a spaceborne radiometer compared with only meters to tens of meters for a SAR. Estimating soil moisture with microwave radiometry is discussed in Chapter 12.

10-6 SMART (Soil Moisture Assessment Radar Technique)

Dubois et al. (1995a, 1995b) developed a soil moisture inversion model that we have named the ***Soil Moisture Assessment Radar Technique***, or SMART for short. The model is based on a data set that combines the University of Michigan measurements made by the LCX POLARSCAT (Tassoudji et al., 1989) and the measurements made by the RASAM systems (Wegmüller, 1993) at the University of Berne in

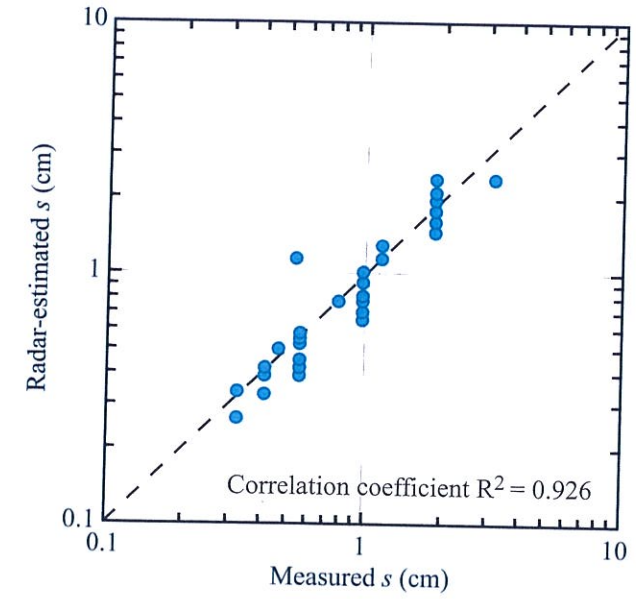

(a) rms height s

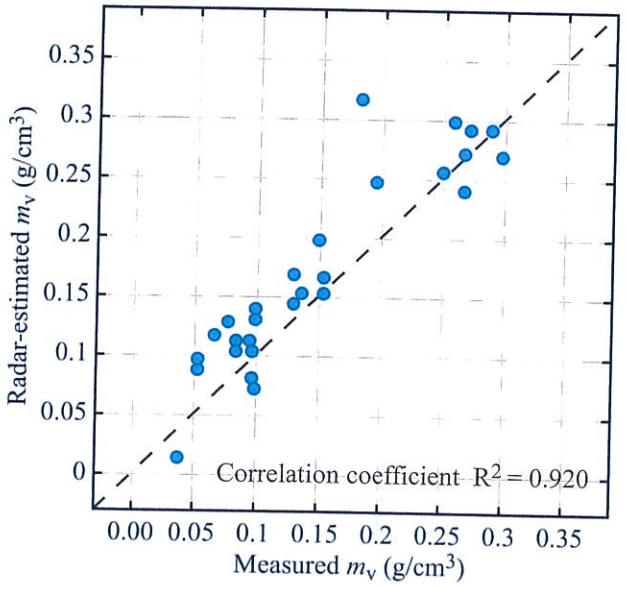

(b) Volumetric moisture content m_v

Figure 10-37: To reduce the scattering in Fig. 10-36 due to intercalibration among the various radars and measurement campaigns, multifrequency/angle radar estimates are averaged together [Oh, 2004].

Switzerland. The first of these two data sets led to the development of the PRISM model described in the preceding section. It included measurements at three microwave frequencies (1.25, 4.75, and 9.5 GHz) for multiple surfaces with rms height s varying from 0.32 cm to 3.02 cm. The second data set included measurements at six frequencies between 2.5 and 11 GHz for surfaces with rms height varying from 0.57 cm to 1.12 cm. Both data sets included soil moisture and soil density measuruments.

Using these data sets for $\theta \geq 30°$, the SMART model offers the following empirical relationships:[¶†]

$$\sigma^0_{hh} = 10^{-2.75} \cdot \frac{\cos^{1.5}\theta}{\sin^5\theta} \cdot 10^{0.028\varepsilon' \tan\theta} (ks \sin\theta)^{1.4} \lambda^{0.7}, \tag{10.41a}$$

$$\sigma^0_{vv} = 10^{-2.35} \cdot \frac{\cos^3\theta}{\sin^3\theta} \cdot 10^{0.046\varepsilon' \tan\theta} (ks \sin\theta)^{1.1} \lambda^{0.7}, \tag{10.41b}$$

where ε' is the real part of the soil dielectric constant, $k = 2\pi/\lambda$, s is the rms height in cm, and λ is the wavelength in cm. The units of σ^0_{hh} and σ^0_{vv} are m^2/m^2. Figure 10-38 displays a family of plots of σ^0_{vv} (dB) against the co-pol ratio $p = \sigma^0_{hh}/\sigma^0_{vv}$, with ks and ε' as parameters. The calculations are for $\theta = 45°$. As noted by van Zyl and Kim (2011), the co-pol ratio, based on the model expressions, can exceed 1 for large values of ks, which contradicts theoretical expectations. Hence, the model applicability is better for surfaces with $ks \lesssim 1.2$ than for rougher surfaces.

Aside from the radar parameters θ and λ, both of which are known, the only unknown parameters in Eq. (10.41) are ε' and s. Measured radar values for σ^0_{hh} and σ^0_{vv} are used to determine ε' and s, and then a soil dielectric model (Section 4-8) is used to relate ε' to the soil moisture content m_v.

To demonstrate the viability of the SMART model, Dubois et al. (1995a, 1995b) isolated the term $(ks \sin\theta)$ on the right-hand side of Eq. (10.41) and then converted

[¶]The original paper by Dubois et al. (1995a) included printing errors that were noted in a later correction (1995b).

[†]**Computer Code 10.7.**

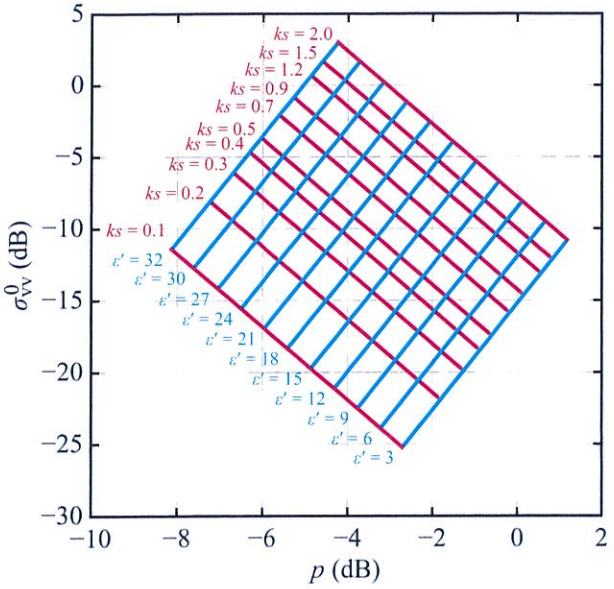

Figure 10-38: SMART model algorithm.

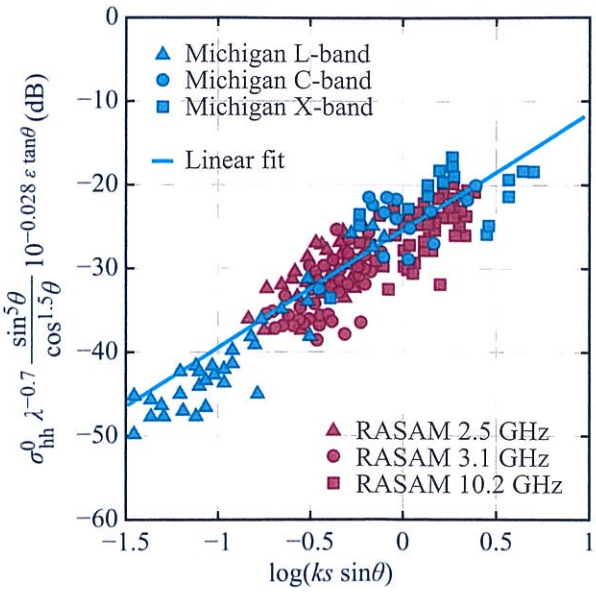

Figure 10-39: Plot of $10\log[\sigma^0_{hh}\lambda^{-0.7}(\sin^5\theta/\cos^{1.5}\theta) \times 10^{-0.028\varepsilon'\tan\theta}]$ as a function of $\log(ks\sin\theta)$ for the POLARSCAT and RASAM scatterometer data [Dubois et al., 1995a, b].

both sides to dB, which leads to

$$10\log\left[\sigma^0_{hh}\lambda^{-0.7}\cdot\frac{\sin^5\theta}{\cos^{1.5}\theta}\cdot 10^{-0.028\varepsilon'\tan\theta}\right] = 10\log[10^{-2.75}(ks\sin\theta)^{1.4}] = -27.5+14\log(ks\sin\theta). \quad (10.42)$$

Figure 10-39 displays the calculated values of the left-hand side of Eq. (10.42), plotted against $\log(ks\sin\theta)$, for the combined data set. The linear form of Eq. (10.42) is represented by the straight line shown in Fig. 10-39. Application of the model in an inverse mode to estimate m_v and s from σ^0_{hh} and σ^0_{vv} leads to the results shown in Fig. 10-40. The reported rms error is on the order of 4% for m_v and 0.4 cm for s. Application of the inverse model to L-band images recorded by airborne and spaceborne imaging radars led to the results displayed in Fig. 10-41.

The inversion equations are given by (van Zyl and Kim, 2011):†

$$\varepsilon' = \frac{1}{3.36\tan\theta}\{14\sigma^0_{vv}\,(\text{dB}) - 11\sigma^0_{hh}\,(\text{dB}) + 26.5 - 255\log_{10}(\cos\theta) - 130\log_{10}(\sin\theta) - 21\log_{10}(\lambda)\}, \quad (10.43a)$$

and

$$\log_{10}(ks) = -0.083\sigma^0_{vv}\,(\text{dB}) + 0.137\sigma^0_{hh}\,(\text{dB}) + 1.807 + 0.446\log_{10}(\cos\theta) + 3.345\log_{10}(\sin\theta) - 0.375\log_{10}(\lambda) \quad (10.43b)$$

with λ in cm.

The SMART model has several attractive features: (a) its expressions are straightforward and easy to use, (b) it relies on only hh and vv polarizations (whereas

† Computer Code 10.8.

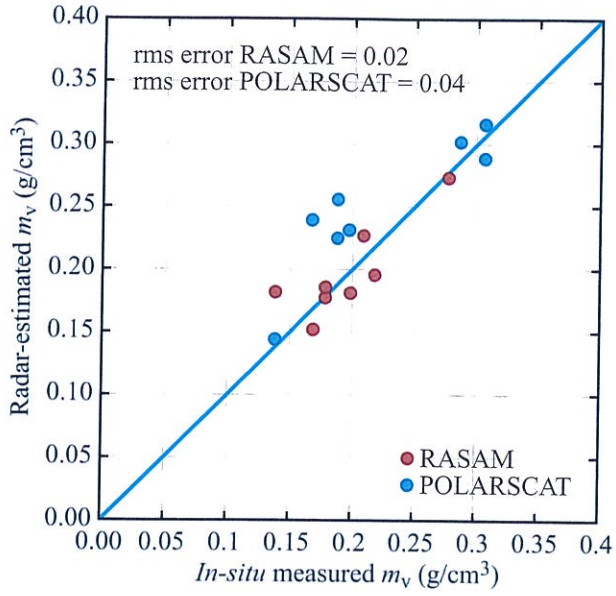

(a) Soil moisture versus *in-situ* measured soil moisture

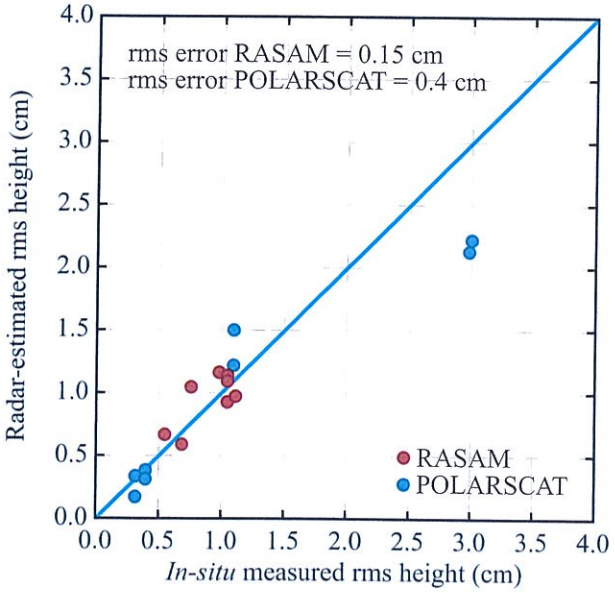

(b) rms height versus *in-situ* measured rms height

Figure 10-40: Estimated (a) soil moisture versus *in-situ* measured soil moisture and (b) rms height versus *in-situ* measured rms height [Dubois et al., 1995a].

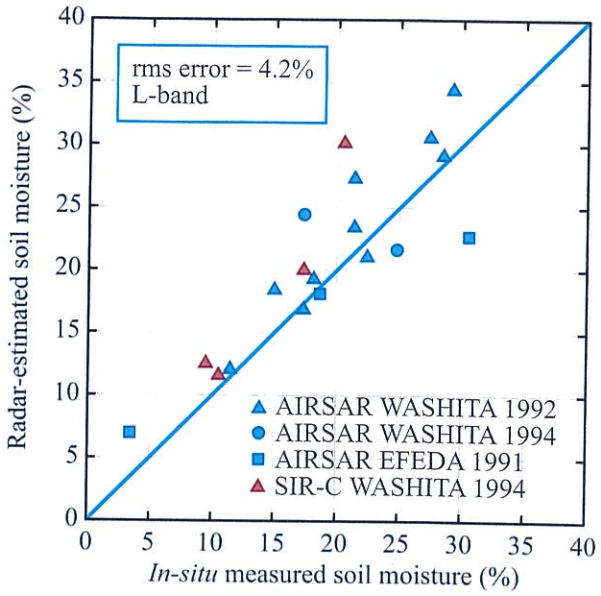

Figure 10-41: Radar-estimated soil moisture versus *in-situ* measured soil moisture for bare-soil fields imaged by the JPL AIRSAR and SIR-C [Dubois et al., 1995a].

the PRISM model uses those two plus σ^0_{hv}), and (c) it provides estimates of m_v and s with good accuracies. Consequently, it has been applied at numerous sites to map soil moisture content on the basis of multipolarized radar imagery (Kseneman and Gleich, 2009; Truong-Loï et al., 2009; Merzouki et al., 2011; Prakash et al., 2012).

10-7 Model Comparisons

EM scattering models are of three varieties. The simplest in form and expression are the semiempirical, and, in the present context, they include the PRISM model of Section 10-5 and the SMART model of Section 10-6. They tend to be of hybrid construction based on experimental data but guided by trends predicted by theoretical models.

The second variety consists of theoretical models that are based on a firmer theoretical foundation, but whose analytical solutions require the imposition of various assumptions to support the use of mathematical

approximations. Often, their solutions require complex integrations, but their computational demands are relatively modest. The I²EM model of Section 10-3 is a perfect example.

The third variety encompasses numerical solutions of Maxwell's equations in 3-D, which are regarded as more exact than the approximate theoretical models, but they are computationally very demanding. In a recent study, Huang et al. (2010) used a method-of-moments technique to compute about 6000 numerical solutions of σ° for hh and vv polarizations and of the emissivity e, also for h and v polarizations, as a function of several surface variables. The surface variables included s/λ, l/λ, and ε, where s and l are the rms height and correlation length of the random surface, and ε is its dielectric constant. All computations were performed at $\theta = 40°$. Their results for σ° are summarized in Figs. 10-42 and 10-43.

Part (a) of Fig. 10-42 displays three curves of σ^0_{vv} as a function of ks, together with six data points. The data points correspond to the numerical method-of-moment 3-D (NMM3D) computation reported by Huang et al. (2010), and the three curves represent the I²EM, PRISM-1, and SMART models. A similar set for σ^0_{hh} is displayed in part (b) of the same figure, and similar comparisons are provided in Fig. 10-43 as a function of ε'.

In a study similar to that reported by Huang et al. (2010), Baghdadi et al. (2011) evaluated the I²EM, PRISM, and SMART models relative to measurements made by the high-resolution TerraSAR-X imaging radar for several sites in France and Tunisia.

10-8 Concluding Observations

Since the publication of the first report examining the radar response to soil moisture (Ulaby, 1974), hundreds of studies have been conducted to quantify the nature of the response and to use that knowledge to develop inversion techniques so as to generate soil-moisture distribution maps on a large scale. We now have the basic tools—embodied in models like I²EM, PRISM, and SMART, but we still need to develop an algorithm capable of generating the desired soil-moisture maps

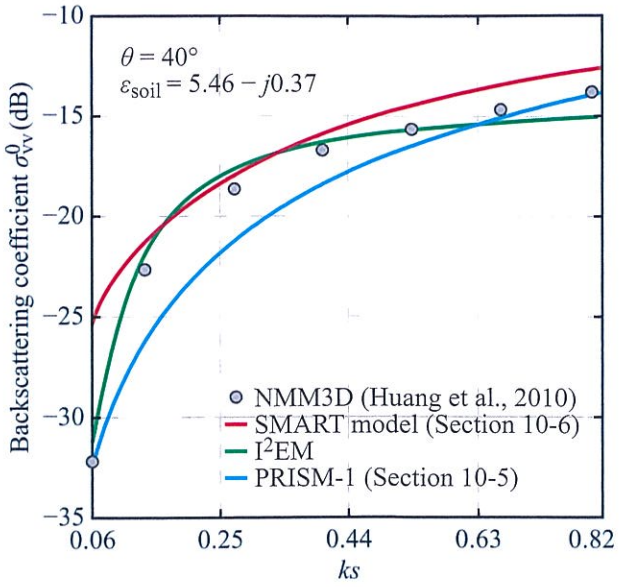

(a) σ^0_{vv}

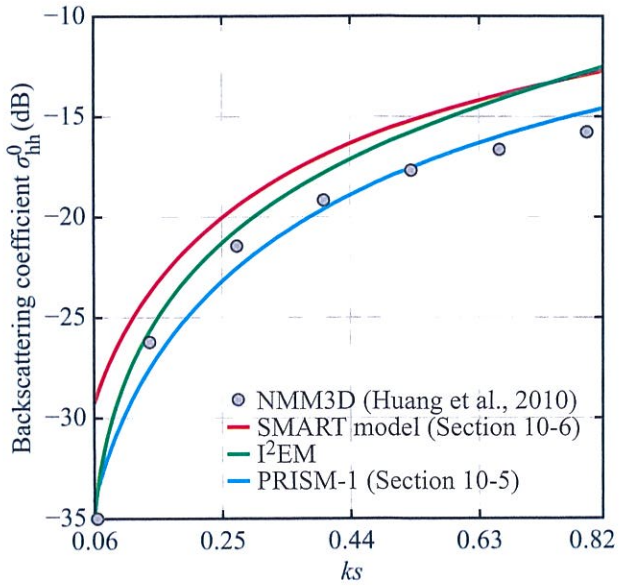

(b) σ^0_{hh}

Figure 10-42: Comparison of numerical 3-D computed values with I²EM, PRISM-1, and SMART models for (a) vv polarization and (b) hh polarization.

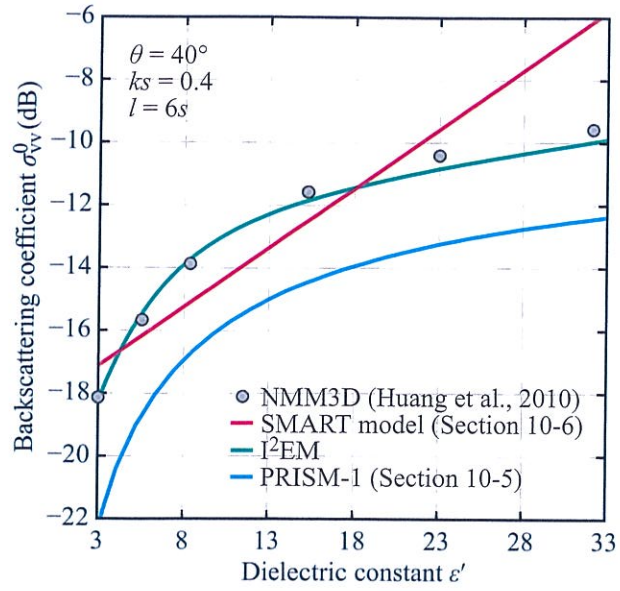

(a) σ^0_{vv}

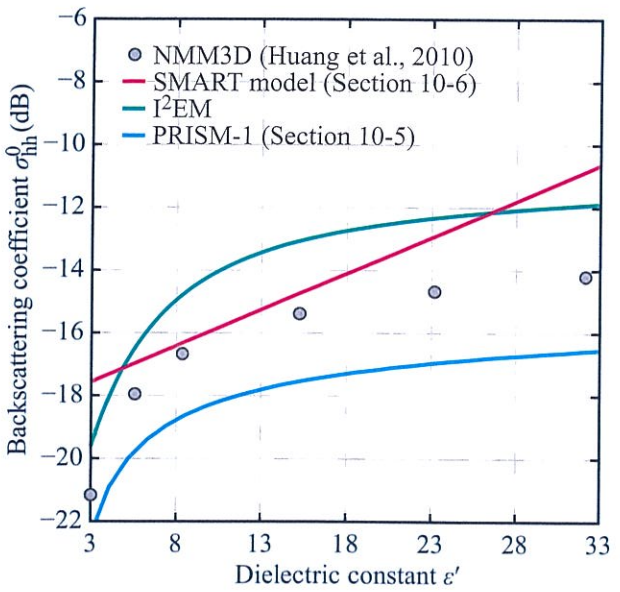

(b) σ^0_{hh}

Figure 10-43: Comparison of numerical 3-D computed values with I²EM, PRISM-1, and SMART models for (a) vv and (b) hh polarizations.

with an acceptable degree of accuracy, on the order of 3–4%. The challenge is two-dimensional. The first dimension has to do with our definition of the soil volumetric moisture content m_v. In some field studies, m_v is measured over the top 1 cm of the soil surface, in others it is over 2 cm or as much as 5 cm. The moisture actually has a profile that may decrease or increase with depth, further complicating the definition of what we mean by m_v. Perhaps the answer to this issue is to designate the m_v predicted by the radar inversion models as a ***radar-equivalent moisture content*** and then let the users of the soil-moisture information (hydrologist, climate modelers, farmers, etc.) figure out how best to use it for their intended applications.

The second challenge has to do with the oversimplification of our description of surface roughness. According to I²EM, the surface-height statistics are governed by the form of the correlation function, the rms height, and the correlation length l, and if the surface-height profile includes multiple scales of roughness, these aforementioned parameters apply to each roughness scale. The PRISM and SMART models rely on ks as the sole representative of roughness. Since different roughness scales respond differently to different wavelengths, a two-frequency polarimetric radar (such as an L-band plus a C-band) is more likely to provide a higher-accuracy estimate of m_v than a single-frequency system can. This was certainly the conclusion reached by the study reported by Oh (2004); compare the results displayed in Fig. 10-36 with those in Fig. 10-37! To sense soil moisture under vegetation cover (as discussed in Chapter 12), it may be necessary to add a third (or even a fourth) lower frequency channel.

PROBLEMS

10.1 Suppose a random surface is characterized by three scales of roughness. Use the results displayed in Fig. 10-9 to explain which roughness scale is the most important and under what conditions. Consider the ratio s_i/λ_e where s_i is the rms height of the ith scale and λ_e is the effective wavelength.

10.2 Consider a three-scale random surface with a Gaussian correlation function. The surface roughness

parameters are $s_1 = 1$ cm, $l_1 = 15$ cm, $s_2 = 0.4$ cm, $l_2 = 5$ cm, $s_3 = 0.2$ cm, and $l_3 = 2.5$ cm. The dielectric constant is $\varepsilon = 12$. Compute the backscattering coefficient for hh polarization at $\theta = 30°$ and plot it as a function of ks, where k is the wavenumber and s is the equivalent rms height of the surface. The range of ks should extend from 0.1 to 1.

10.3 Figure 10-13 contains a plot for σ^0_{hv} as a function of m_v at $f = 3$ GHz. Generate similar plots for the same surface at 1.5 GHz and 4.5 GHz.

10.4 Consider a one-dimensional sinusoidal surface with $A = 8$ cm and $\Lambda = 40$ cm. Superimposed on the periodic surface is a relatively smooth random surface with backscattering coefficient (in the absence of the periodic surface) given by

$$\sigma^s_{vv} = e^{-13.2\theta'} \qquad (m^2/m^2),$$

where θ' is the incidence angle in radians. Compute and plot the backscattering coefficient that would be observed by an imaging radar (with a spatial resolution many times greater than Λ) at incidence angle $\theta_0 = 20°$. Your plot should show the variation with the azimuth angle ϕ_0 (0 to 180°).

10.5 Repeat Problem 10.4 for a relatively rough random surface with

$$\sigma^s_{vv} = e^{-2\theta'} \qquad (m^2/m^2).$$

10.6 Use Computer Codes 4.7 and 10.5 to compute the PRISM-1 model variations with m_v (0 to 0.3 g/cm^3) for:

(a) σ^0_{vv}

(b) σ^0_{hh}

(c) σ^0_{hv}

(d) co-pol and cross-pol ratios.

Assume $f = 3$ GHz, $\theta = 45°$, and $s = 1.5$ cm.

10.7 Use Computer Codes 4.7 and 10.7 to generate SMART model variations with m_v (0 to 0.3 g/cm^3) for:

(a) σ^0_{vv}

(b) σ^0_{hh}

Assume $f = 3$ GHz, $\theta = 45°$, and $s = 1.5$ cm.

10.8 A 1.5 GHz polarimetric radar is used to image bare-soil fields at an incidence angle of 30°. The soil dielectric constant is given by the approximate model

$$\varepsilon' = 57m_v + 3,$$
$$\varepsilon'' = 11m_v,$$

where m_v is in g/cm^3. Use the PRISM-1 forward model to generate a database for σ^0_{hh} and σ^0_{vv} for various combinations of m_v and the rms height s over the ranges $0.05 \le m_v \le 0.35$ g/cm^3 and $0.2 \le s \le 2$ cm. Use the database to develop an inverse model. Evaluate your model performance by performing a linear-regression analysis to compare the values of m_v predicted by the model with the true values of m_v.